Check for updates

ABHD17 regulation of plasma membrane palmitoylation and N-Ras-dependent cancer growth

Jarrett R. Remsberg [1,6], Radu M. Suciu[1,6], Noemi A. Zambetti[2,3,6], Thomas W. Hanigan[1],
Ari J. Firestone [2,3], Anagha Inguva[2], Amanda Long[2], Nhi Ngo[4], Kenneth M. Lum[4],
Cassandra L. Henry[4], Stewart K. Richardson[5], Marina Predovic[2], Ben Huang [2,3], Melissa M. Dix[1],
Amy R. Howell[5], Micah J. Niphakis [4 ✉], Kevin Shannon [2,3 ✉] and Benjamin F. Cravatt [1 ✉]

Multiple Ras proteins, including N-Ras, depend on a palmitoylation/depalmitoylation cycle to regulate their subcellular trafficking and oncogenicity. General lipase inhibitors such as Palmostatin M (Palm M) block N-Ras depalmitoylation, but lack specificity and target several enzymes displaying depalmitoylase activity. Here, we describe ABD957, a potent and selective covalent inhibitor of the ABHD17 family of depalmitoylases, and show that this compound impairs N-Ras depalmitoylation in human acute myeloid leukemia (AML) cells. ABD957 produced partial effects on N-Ras palmitoylation compared with Palm M, but was much more selective across the proteome, reflecting a plasma membrane-delineated action on dynamically palmitoylated proteins. Finally, ABD957 impaired N-Ras signaling and the growth of *NRAS*-mutant AML cells in a manner that synergizes with MAP kinase kinase (MEK) inhibition. Our findings uncover a surprisingly restricted role for ABHD17 enzymes as regulators of the N-Ras palmitoylation cycle and suggest that ABHD17 inhibitors may have value as targeted therapies for *NRAS*-mutant cancers.

*R*AS genes are the most common targets of dominant mutations in human cancer[1]. There are three different *RAS* genes, which encode four highly homologous proteins (H-Ras, N-Ras, K-Ras4a and K-Ras4b)[1]. An elegant approach for directly targeting Ras oncoproteins involves designing covalent inhibitors targeting cysteine 12 of K-Ras[G12C] (refs. [2,3]). However, it is more challenging to apply this approach to oncogenic amino acid substitutions that introduce side chains lacking reactive nucleophiles.

Ras proteins share high homology throughout most of their protein sequence with the exception of the C-terminal 'hypervariable region' (HVR), which contains signals that specify post-translational modifications required for proper subcellular localization[4]. The HVR of all four isoforms terminates with a CAAX motif, where the cysteine is prenylated by farnesyltransferases. This lipid modification provides weak membrane-binding affinity that is stabilized by a second signal motif. For K-Ras4b, this is provided by a polybasic lysine domain[5]. By contrast, H-Ras, N-Ras and K-Ras4a are *S*-palmitoylated at cysteine(s) adjacent to the CAAX motif[4,5], and a dynamic cycle of palmitoylation and depalmitoylation mediated by palmitoyl acyl transferase and depalmitoylase enzymes, respectively, has been shown to regulate H- and N-Ras trafficking, subcellular localization and function[6,7].

The enzymes involved in depalmitoylating H- and N-Ras are presumed to be serine hydrolases based on studies showing that N-Ras depalmitoylation is blocked by the β-lactone small molecules Palmostatin B (**1**) and M (**2**) (Palm B and M)[7,8] or hexadecylfluorophosphonate (HDFP, **3**) (ref. [9]), as well as earlier work demonstrating that the yeast serine hydrolase APT1 (or, in humans, LYPLA1) can depalmitoylate H-Ras[10]. While LYPLA1 and LYPLA2 are inhibited by Palm B and M[11], selective inhibitors or genetic knockdown

of these serine hydrolases does not affect the palmitoylation dynamics of N-Ras in cancer cells[12], pointing to other enzymes being involved in this process. Activity-based protein profiling (ABPP) methods were recently used to identify ABHD17 enzymes, a poorly characterized group of three sequence-related serine hydrolases (ABHD17A, B and C, or the ABHD17s), as additional targets of Palm M and HDFP, and these enzymes can depalmitoylate N-Ras[12]. The ABHD17s are themselves palmitoylated on their N-termini, which promotes localization to the plasma membrane of cells[13]. Importantly, overexpression of ABHD17A was found to enhance N-Ras depalmitoylation and altered N-Ras subcellular localization in COS-7 cells, and, conversely, triple knockdown of ABHD17A/B/C by RNA interference impaired N-Ras palmitoylation turnover, albeit less effectively than Palm B, in HEK293T cells[12].

Previous findings, taken together, support a potential role for ABHD17s in regulating N-Ras palmitoylation. However, ABHD17A, B and C are all broadly expressed in most cell types, which makes characterization of their collective contribution to N-Ras palmitoylation challenging using genetic methods. Additionally, studies performed to date relating ABHD17s to N-Ras depalmitoylation have occurred in heterologous cell types that do not depend on N-Ras as an oncogenic driver. Accordingly, it remains unknown whether ABHD17s regulate N-Ras palmitoylation in relevant biological systems and if disrupting these enzymes will affect the growth of *NRAS*-mutant cancer cells. Finally, the broader potential substrate scope of ABHD17 enzymes beyond N-Ras and a handful of other palmitoylated proteins (for example, PSD-95; refs. [12,14]) remains unknown.

To address the aforementioned knowledge gaps, we describe herein a potent, selective and cell-active covalent inhibitor of

[1]Department of Chemistry, The Scripps Research Institute, La Jolla, CA, USA. [2]Department of Pediatrics, University of California, San Francisco, San Francisco, CA, USA. [3]Helen Diller Family Comprehensive Cancer Center, University of California, San Francisco, San Francisco, CA, USA. [4]Lundbeck La Jolla Research Center, Inc., San Diego, CA, USA. [5]Department of Chemistry, University of Connecticut, Storrs, CT, USA. [6]These authors contributed equally: Jarrett R. Remsberg, Radu M. Suciu, Noemi A. Zambetti. ✉e-mail: MIIP@lundbeck.com; Kevin.Shannon@ucsf.edu; cravatt@scripps.edu

ABHD17s. We find that this compound, termed ABD957 (**4**), inhibits all three ABHD17s and partially impairs N-Ras depalmitoylation, extracellular signal-regulated kinase (ERK) phosphorylation and the growth of *NRAS*-mutant cancer cells. ABD957 stabilizes N-Ras palmitoylation less completely than Palm M, but is much more selective across the proteome, being restricted in its effects to plasma membrane-associated, dynamically palmitoylated proteins. ABD957 and Palm M also differentially impacted the subcellular distribution of N-Ras, leading to accumulation of this protein at the plasma membrane and intracellular membranes, respectively. Finally, we show that ABD957 synergizes with MEK inhibition to block *NRAS*-mutant cancer cell growth and that ABD957 pharmacological effects are abrogated in cells lacking ABHD17A and ABHD17B. These data, taken together, indicate that ABHD17s perform a specialized function as plasma membrane-delineated *S*-depalmitoylases and that chemical inhibition of these enzymes attenuates dynamic N-Ras depalmitoylation, resulting in impaired signaling and growth of *NRAS*-mutant cancer cells.

Results

Discovery and characterization of ABHD17 inhibitors. The palmostatins (Palm B and Palm M)[7,8] and HDFP[9] (Fig. 1a) are useful pharmacological tools for studying protein palmitoylation through blockade of depalmitoylase enzymes and, to date, remain the only reported inhibitors of ABHD17A/B/C[12]. HDFP is a broad-spectrum serine hydrolase inhibitor, targeting multiple depalmitoylases including LYPLA1/2, PPT1, ABHD10 and ABHD17A/B/C[9]. This compound[9,15,16], along with other long-chain fluorophosphonates (FPs)[17,18], has been shown to preserve the palmitoylation state of several dynamically palmitoylated proteins, including Ras proteins[9,12], in mammalian cells. Palm B and Palm M also inhibit several other serine hydrolases[11,12], and this lack of selectivity, along with the presence of a metabolically labile β-lactone, has limited the broad utility of these compounds in biological systems. Such factors motivated us to develop a more advanced chemical probe that selectively inhibits ABHD17 enzymes (ABHD17s).

HDFP and palmostatins feature reactive electrophilic centers that inhibit serine hydrolases through covalent modification of the catalytic serine residue. While this feature likely contributes to a lack of specificity across the serine hydrolase class, more tempered electrophiles, such as carbamates and ureas, have been shown to covalently inhibit individual serine hydrolases with excellent potency and selectivity[19–21]. The evaluation of candidate inhibitors of serine hydrolases has also benefited from the chemical proteomic technology ABPP, wherein activity-based probes showing broad reactivity with serine hydrolases are used to measure target engagement and selectivity of inhibitors in native biological systems[22]. We accordingly screened a serine hydrolase-directed compound library internally developed at Lundbeck La Jolla Research Center, Inc. (~5,000 compounds screened in total) using gel-based ABPP in native mouse brain proteomes, where ABHD17s and other serine hydrolases can be visualized using a fluorescently (rhodamine) tagged FP activity-based probe (Supplementary Table 1). This screen furnished a piperazine-based pyrazole urea hit (compound **5**, Fig. 1b) that displayed moderate potency (IC$_{50}$ (95% CI) = 0.89 (0.71–1.1) μM; Supplementary Table 2 and Extended Data Fig. 1a,b) against human ABHD17B, assayed by gel-based ABPP in stably transduced HEK293T cells.

Compound **5** represented an attractive starting point because of its simple, chemically tractable core and the presence of a moderately electrophilic pyrazole urea group resembling those found in other advanced chemical probes that covalently inhibit serine hydrolases[19,21,23]. We next used a biotinylated FP probe[24] and quantitative MS-ABPP to assess the selectivity of **5** in the proteome of the human *NRAS*-mutant AML cell line OCI-AML3 (Supplementary Dataset 1). Experiments performed with 1 and 10 μM of **5** confirmed inhibition of the ABHD17s, as well as several additional serine hydrolases,

including LYPLA1 and LYPLA2 (Fig. 1c and Extended Data Fig. 1c). Through iterative ABPP-guided medicinal chemistry, we eliminated LYPLA1/2 activity while simultaneously improving inhibitory potency and selectivity for ABHD17s. Introduction of a morpholino group on the benzyl moiety and replacement of the chlorine with a trifluoromethyl group (compound **6**, Fig. 1b), followed by shifting the sulfonamide from the 4-position to the 3-position on the pyrazole leaving group, decreased potency for LYPLA1 and concurrently enhanced ABHD17B potency (compound **7**, Fig. 1b; IC$_{50}$ (95% CI) = 0.25 (0.20–0.32) μM) (Supplementary Table 2). MS-based ABPP experiments revealed that these modifications also had a favorable impact on overall selectivity, removing off-targets such as ABHD4 and ABHD11 (Fig. 1c and Extended Data Fig. 1c). Reasoning that increasing the steric demand around the electrophile could further improve selectivity[20,21], we introduced a methyl substituent on the piperazine staying group adjacent to the urea (compound **8**, Fig. 1b), which boosted potency (IC$_{50}$ (95% CI) = 0.14 (0.11–0.16) μM, Supplementary Table 2) and shifted the selectivity profile: eliminating PAFAH2, but introducing ABHD10, a recently identified mitochondrial depalmitoylase[18], as an off-target (Fig. 1c and Extended Data Fig. 1c). Furthermore, **8** suffered from poor metabolic stability in human liver microsomes (480 μl min^{-1} mg^{-1}, Supplementary Table 2) and, when tested in cells, did not produce sustained inhibition of ABHD17s over 72 h (Fig. 1d), a common endpoint used for cell-based assays that measure, for instance, proliferation.

Additional modifications to **8** furnished the more advanced chemical probe ABD957 (compound **4**, Fig. 1b) that displayed much lower microsomal clearance (4.8 μl min^{-1} mg^{-1}, Supplementary Table 2) while maintaining good potency for ABHD17B (IC$_{50}$ (95% CI) = 0.21 (0.16–0.28) μM, Fig. 1e, Extended Data Fig. 1b and Supplementary Table 2) and selectivity, including avoidance of ABHD10 as an off-target (Fig. 1c and Extended Data Fig. 1c). We also performed MS-based ABPP experiments on OCI-AML3 cells treated in situ with ABD957 (500 nM) for 2 h (Fig. 1f), which revealed 90% plus blockade of ABHD17s with good overall selectivity, including no cross-reactivity with LYPLA1, LYPLA2 or ABHD10. While ABD957 inhibited a handful of other serine hydrolases, including CES1/2, ABHD6 and ABHD13, global selectivity was markedly improved compared with previous ABHD17 inhibitors, such as Palm M and HDFP, which, consistent with previous studies[9,12], caused widespread serine hydrolase inhibition in cells (Extended Data Fig. 1d). Also, we identified inactive control compounds, JJH254 (**9**)[25] and ABD298 (**10**), that inhibited the majority of off-targets of ABD957, while leaving the ABHD17s unperturbed (Extended Data Fig. 2a–d). Importantly, ABD957 (1 μM) produced sustained cellular inhibition of ABHD17A/B/C for 72 h (Fig. 1d), indicating that this compound was well-suited for a diverse array of cell-based experiments.

ABD957 attenuates N-Ras depalmitoylation in AML cells. To assess the impact of ABHD17 inhibition on N-Ras palmitoylation, we adapted a pulse–chase assay for measuring dynamic protein palmitoylation[9]. We first generated sublines of OCI-AML3 cells in which we used RNA interference to reduce the expression of endogenous human N-Ras and then introduced into these cells either: (1) a murine green fluorescent protein (GFP)–N-Ras^{G12D} protein, or (2) a murine GFP–N-Ras^{G12D} variant in which the palmitoylated HVR sequence was replaced with the nonpalmitoylated HVR sequence of K-Ras4b (Supplementary Fig. 1). The two engineered cell lines expressing GFP–N-Ras^{G12D} and GFP–N-Ras$^{G12D, KRAS\ HVR}$ proteins, termed 'ON' and 'ONK', respectively, were expected to retain (ON) or lose (ONK) dependency on the palmitoylation of mutant N-Ras for signaling and growth (we have shown in previous studies that an oncogenic form of N-Ras loses transforming activity when the C181 palmitoylation
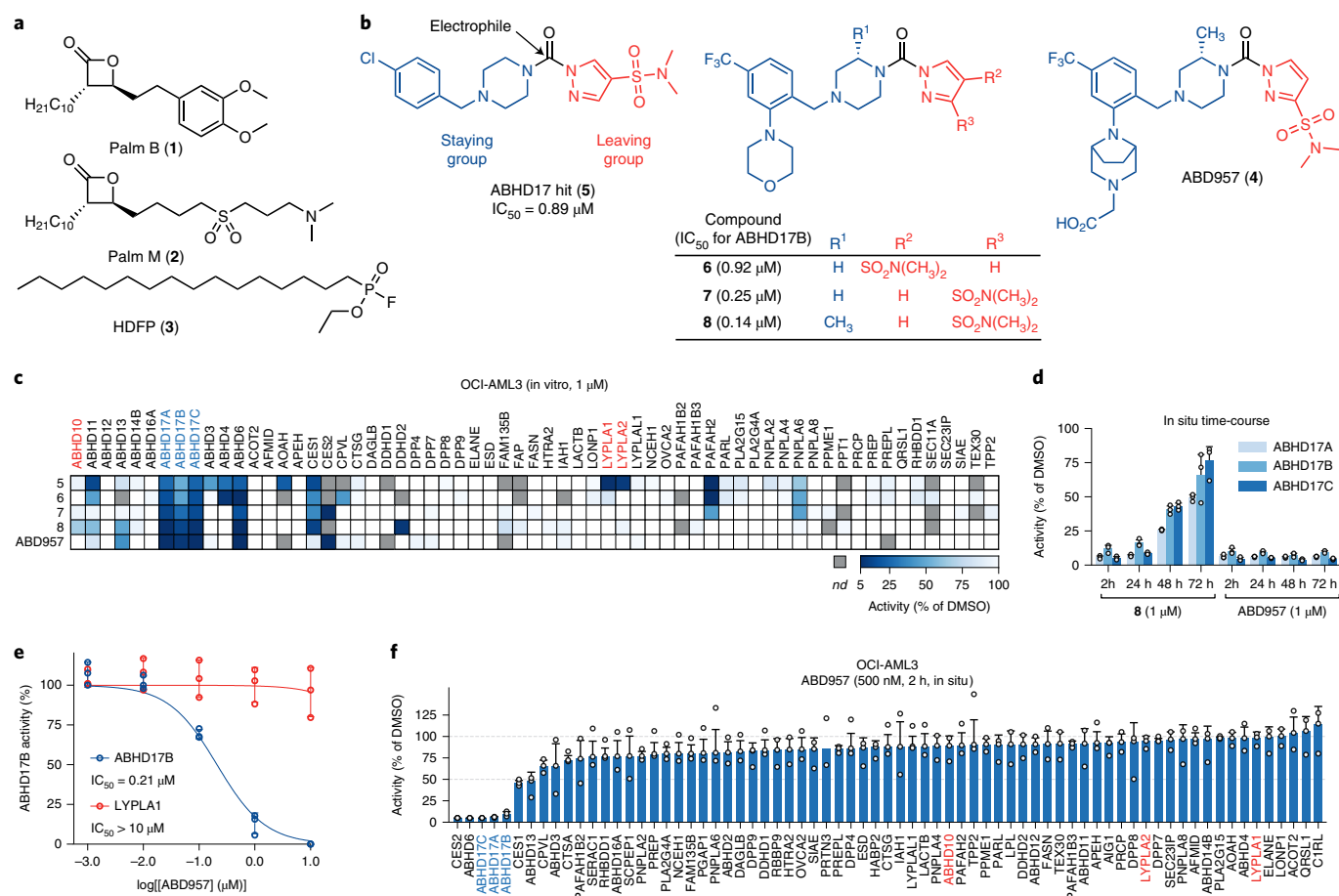
Fig. 1 | Discovery and characterization of ABD957: a potent and selective inhibitor of the ABHD17 enzymes. a, Structures of broad-spectrum serine hydrolase inhibitors Palm B, Palm M and HDFP. **b**, Structures of pyrazole urea class of ABHD17 inhibitors discovered herein, highlighting proposed site of covalent reactivity with the active-site serine residue of ABHD17 enzymes. **c**, Mass spectrometry-based ABPP (MS-ABPP) data of serine hydrolase activities in the particulate fraction of OCI-AML3 proteomes treated with compounds **5–8** and ABD957 (1 μM, 30 min). See Extended Data Fig. 1c for MS-ABPP data of compounds tested at 10 μM and Supplementary Dataset 1 for detailed proteomic data. MS-ABPP data are from single experiments performed at the indicated concentrations for each compound. **d**, Targeted MS-ABPP data for an in situ time course of ABHD17A/B/C inhibition by compound **8** and ABD957 (1 μM) in ONK cells, revealing persistent inhibition of ABHD17A/B/C over 72 h in cells treated with ABD957, but not with compound **8**. Data are plotted from biological replicates, and error bars represent s.d. and center around the average (n = 3 independent experiments). **e**, Half maximal inhibitory concentration (IC$_{50}$) curves for ABD957 inhibition of human ABHD17B (recombinantly expressed) and LYPLA1 (endogenous) activity in lysates of HEK293T cells (in vitro) measured by gel-ABPP. Data represent average values ± s.d. (n = 3 independent experiments). **f**, In situ MS-ABPP data for ABD957 (500 nM, 2 h) in OCI-AML3 cells confirming ABHD17A/B/C inhibition and selectivity across the majority of quantified serine hydrolases, including LYPLA1, LYPLA2 and ABHD10. Data plotted represent the median from biological replicates, and error bars represent s.d. (n = 3 independent experiments).

site is mutated[26]). We next evaluated the effect of ABD957 and other compounds on N-Ras palmitoylation dynamics by preincubating ON or ONK cells with compounds or dimethylsulfoxide (DMSO) control for 1 h, then treating cells with the palmitate analog 17-octadecynoic acid (17-ODYA[13,27]; 20 μM) for 1 h, followed by a 1-h chase period in which the media was changed to remove 17-ODYA and supplemented with fresh inhibitor (Extended Data Fig. 3, left and middle panels). The palmitoylation state of N-Ras was then determined by anti-GFP immunoprecipitation, on-bead copper-catalyzed azide–alkyne cycloaddition (CuAAC)[28] to a rhodamine-azide (Rh-N$_3$) reporter tag, and SDS–polyacrylamide gel electrophoresis (SDS–PAGE) and in-gel fluorescence scanning (Extended Data Fig. 3, right lower panel). We also used a similar experimental protocol to survey the proteome-wide effects of candidate depalmitoylation inhibitors by performing CuAAC with Rh-N$_3$ on lysates from 17-ODYA-treated cells (Extended Data Fig. 3, right upper panel).

Consistent with previous studies[7–9,12], we found that the promiscuous lipase inhibitors Palm M and HDFP near-completely preserved N-Ras palmitoylation following the chase period (Fig. 2a,b). ABD957 also protected N-Ras from depalmitoylation, but to a lesser degree than Palm M or HDFP (Fig. 2a,b). By contrast, the control compounds JJH254 and ABD298 did not affect N-Ras palmitoylation dynamics, either alone or in combination with ABD957 (Fig. 2a,b). As expected, palmitoylation signals were not observed in ONK cells (Fig. 2a,c), indicating that the GFP–N-Ras^G12D, KRAS HVR protein does not undergo palmitoylation.

The partial stabilization of N-Ras palmitoylation observed with ABD957 was concentration dependent with an half maximum effective concentration (EC$_{50}$) of 29 nM (Fig. 2c,d), which is consistent with the 90% plus inhibition of ABHD17s in cells treated with 500 nM of this compound (Fig. 1f). Initial proteome-wide surveys of palmitoylation dynamics by SDS–PAGE suggested that ABD957 had a more restricted impact on dynamically palmitoylated proteins
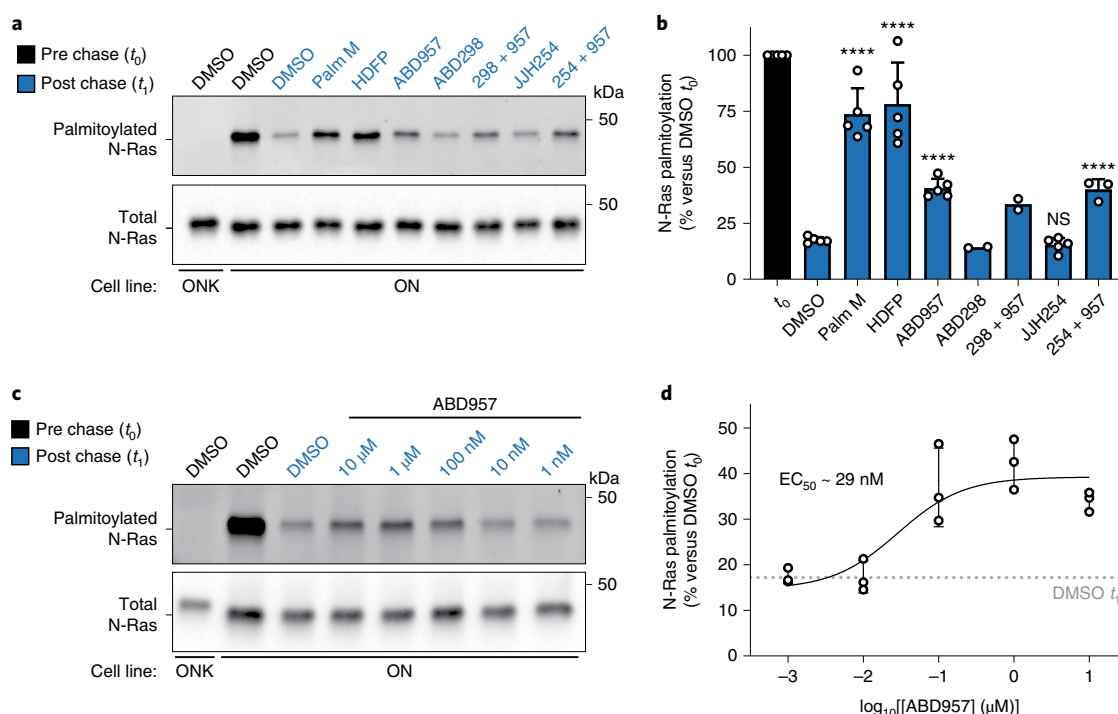
Fig. 2 | Effects of inhibitor treatment on the dynamic palmitoylation state of N-Ras. a, Representative gel measuring N-Ras palmitoylation by 17-ODYA comparing effect of treatment with Palm M (10 μM), HDFP (20 μM), ABD957 (500 nM), ABD298 (500 nM) and JJH254 (1 μM) in OCI-AML3 cells stably expressing GFP–N-Ras^{G12D} (ON) with GFP–N-Ras$^{G12D, KRAS HVR}$ (ONK) as a control (upper panel). Samples co-treated with ABD957 and ABD298 or JJH254 are abbreviated as 298 + 957 and 254 + 957, respectively. The gel is representative of five independent experiments (only one including ABD298, three including JJH254 and five for all other conditions). N-Ras was immunoprecipitated via GFP and the degree of palmitoylation visualized by rhodamine attached via CuAAC to the alkyne of 17-ODYA. Total N-Ras content was measured by western blotting of GFP enrichments (lower panel). **b**, Quantification of inhibitor effects on dynamic palmitoylation. Data represent average values ± s.d. (biological replicates; $n = 2$ for ABD298 and ABD298 + ABD957 samples, $n = 3$ for JJH254 + ABD957 samples and $n = 5$ for all others). Statistical significance was calculated using unpaired two-tailed Student's t-test with equal variance. ****$P < 0.0001$ represents a significant increase compared with DMSO t_1. P values were 4.9×10^{-6} (Palm M), 8.3×10^{-5} (HDFP), 2.5×10^{-6} (ABD957), 0.19 (JJH254) and 3.9×10^{-5} (JJH254 + ABD957). NS, not significant. **c**, Representative gel (from three independent experiments) measuring N-Ras palmitoylation by 17-ODYA in the presence of varying concentrations of ABD957 (upper panel). N-Ras was enriched and visualized as described in **a**. Total N-Ras content was measured by western blotting of GFP enrichments (lower panel). **d**, Quantification of concentration-dependent effects of ABD957 on N-Ras palmitoylation. Data are plotted from biological replicates, and error bars represent s.d. and center around the mean ($n = 3$ independent experiments). Dotted line represents mean of residual post-chase DMSO (t_1) signal.

compared with Palm M or HDFP (Supplementary Fig. 2). Intrigued by these distinct profiles, we next evaluated compounds for effects on global protein palmitoylation by MS-based proteomics.

ABHD17s regulate plasma membrane palmitoylation. We evaluated the impact of compounds on global palmitoylation dynamics using a similar pulse–chase protocol to that previously described[9] and shown in Extended Data Fig. 3, where 17-ODYA-labeled proteins were conjugated by CuAAC to a biotin-N$_3$ tag for streptavidin enrichment followed by quantitative, multiplexed MS-based proteomics using tandem mass tagging (TMT). 17-ODYA-labeled proteins were required to show sensitivity in their enrichment to hydroxylamine treatment (Supplementary Dataset 2) for designation as palmitoylated proteins[29]. In total, 1,227 palmitoylated proteins were identified in OCI-AML3 cells (Supplementary Dataset 2). Consistent with past studies[9,16] only a modest subset of these proteins (22 in total), which included N-Ras, displayed clear evidence of dynamic palmitoylation, as reflected by at least 3-fold reductions in 17-ODYA modification following the 1-h chase period ($t_0/t_1 \geq 3$) (Fig. 3a,b, green and red proteins rightward of vertical dashed red line and Supplementary Dataset 3). The palmitoylation state of most of these proteins was stabilized by treatment with Palm M (10 μM) (Fig. 3a, red proteins and Supplementary Dataset 3). By contrast,

ABD957 (500 nM) preserved the palmitoylation state of only a few select proteins, including N-Ras (Fig. 3b, red proteins). Palm M, but not ABD957, also increased the apparent palmitoylation state of an additional set of proteins that did not show evidence of dynamic palmitoylation (Fig. 3a, blue proteins and Extended Data Fig. 4a). We are unsure of the mechanistic basis for these changes, but they point to a much broader effect of Palm M on the palmitoylated proteome compared with ABD957.

In agreement with our focused palmitoylation assays on N-Ras (Fig. 2), the palmitoylation state of this protein was preserved by both ABD957 and Palm M, with the latter compound showing a greater effect (Fig. 3c). Concordant changes in N-Ras signals were found in both OCI-AML3 and ON cells using either peptides that are unique to N-Ras (relative to other Ras isoforms; for both OCI-AML3 and ON cells) or peptides from the fused GFP protein as a surrogate (for ON cells) (Fig. 3b,c, Extended Data Fig. 4b–d and Supplementary Dataset 3). We also confirmed using an MS-based proteomic pulse–chase stable isotope labeling protocol[30] that, at the time points when ABD957 stabilized N-Ras palmitoylation, the cellular abundance of endogenous N-Ras was unaltered (Extended Data Fig. 5 and Supplementary Dataset 4).

When considering possible reasons why ABD957 did not impact other palmitoylated proteins regulated by Palm M, we noted that
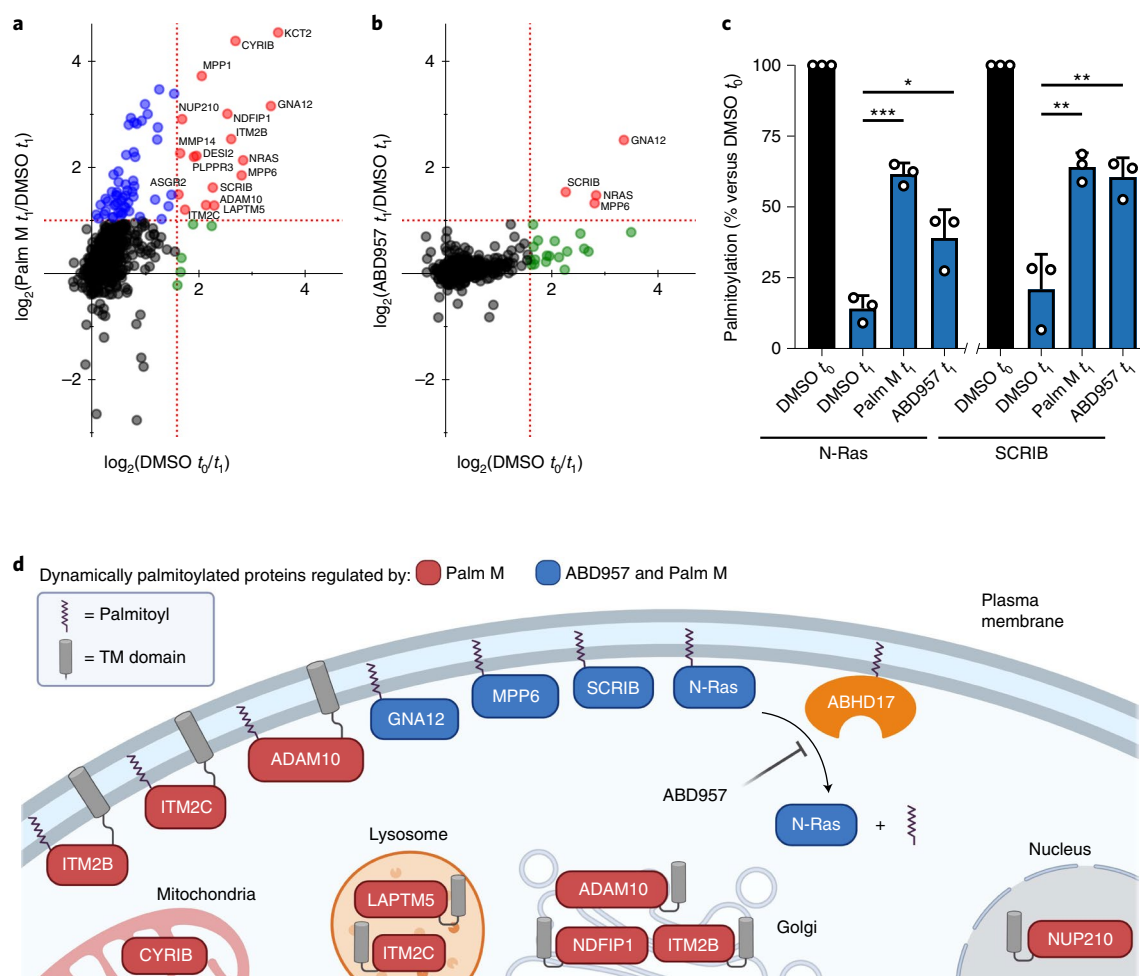
Fig. 3 | Global palmitoylation effects of Palm M and ABD957 in leukemia cells. a,b, MS-based profiling of OCI-AML3 cells as described in Extended Data Fig. 3. Cells were preincubated with Palm M ($10\,\mu M$) or ABD957 ($500\,nM$) for $1\,h$, metabolically labeled with $20\,\mu M$ 17-ODYA for $1\,h$ (t_0) and chased with media lacking 17-ODYA for $1\,h$ (t_1) containing Palm M ($10\,\mu M$, **a**), ABD957 ($500\,nM$, **b**) or DMSO control. Scatter plots compare $\log_2$(fold change) of palmitoylated proteins in experiments measuring dynamic palmitoylation (DMSO t_0/t_1; x axis) versus the effect of inhibitor treatment (inhibitor t_1/DMSO t_1; y axis). Proteins shown were designated as palmitoylated based on their sensitivity to hydroxylamine ($\geq 75\%$ reduction in enrichment following hydroxylamine treatment) as reported in Supplementary Dataset 2. Proteins in red are both dynamically palmitoylated (DMSO $t_0/$ DMSO $t_1 \geq 3$-fold) and preserved in their palmitoylation state by inhibitor treatment (inhibitor t_1/DMSO $t_1 \geq 2$-fold), proteins in green are dynamically palmitoylated, but not preserved by inhibitor treatment (inhibitor t_1/DMSO $t_1 < 2$-fold), and proteins in blue did not display evidence of dynamic palmitoylation (DMSO t_0/DMSO $t_1 < 3$-fold), but showed higher palmitoylation signals following inhibitor treatment (inhibitor t_1/DMSO $t_1 \geq 2$-fold). Red dotted lines represent 2- and 3-fold ratio values for y and x axes, respectively. Data represent average values ($n = 3$ biological replicates). HLA proteins not shown. **c**, Bar graphs quantifying N-Ras (left) and SCRIB (right) palmitoylation from MS-based proteomic experiments. Data represent average values relative to DMSO $t_0 \pm$ s.d. ($n = 3$ biological replicates). Statistical significance was calculated with unpaired two-tailed Student's t-test with equal variance, *$P < 0.05$, **$P < 0.01$, ***$P < 0.001$ represent significant increase compared with DMSO t_1. P values were 1.6×10^{-4} (Palm M N-Ras), 0.0173 (ABD957 N-Ras), 0.0050 (Palm M SCRIB) and 0.0084 (ABD957 SCRIB). **d**, Cartoon diagram depicting the subcellular localization of selected proteins showing dynamic palmitoylation that was inhibited by Palm M (red) or both Palm M and ABD957 (blue) (created with BioRender.com). Transmembrane domains are annotated by PSORT II[48].

the four main proteins affected by ABD957 all reside at the plasma membrane (Fig. 3d) including, in addition to N-Ras: SCRIB (Fig. 3b,c), a scaffolding protein that depends on palmitoylation for plasma membrane localization and function[31]; MPP6, a palmitoylated guanylate kinase that has been shown to localize to the basolateral plasma membrane of intestinal epithelial cells[32]; and GNA12, a palmitoylated guanine nucleotide-binding protein that plays a role in Rho signaling[33]. By contrast, dynamically palmitoylated proteins affected by Palm M, but not ABD957, localized to other subcellular compartments (for example, Golgi (NDFIP1), nucleus (NUP210), lysosome (LAPTM5), mitochondria (CYRIB)) (Fig. 3d), where they may not interface with plasma membrane-localized ABHD17s.

Some possible exceptions included a handful of Palm M-regulated transmembrane proteins (for example, ADAM10 and ITM2B/C) that localize to both intracellular membrane compartments and the plasma membrane[34,35]. Finally, we also analyzed the effects of depalmitoylation inhibitors on the dynamically palmitoylated proteome of the K-Ras mutant cancer cell line NB-4, which revealed that ABD957 also controlled SCRIB palmitoylation in these cells (Extended Data Fig. 6a and Supplementary Dataset 3). Notably, the dynamic palmitoylation state of wild-type N-Ras was only modestly sensitive to ABD957 in NB-4 cells, despite still being fully preserved by Palm M (Extended Data Fig. 6b and Supplementary Dataset 3). Our quantitative proteomic data thus indicate that the

ABHD17s regulate the dynamic palmitoylation state of mutant N-Ras and a discrete set of plasma membrane-localized proteins in leukemia cells.

ABD957 impacts N-Ras localization in leukemia cells. Previous studies have shown that Palm B and Palm M alter the subcellular localization of N-Ras, leading to redistribution of this protein from the plasma membrane to endomembranes[7,8,36]. This effect was also shown to depend on the presence of the N-Ras HVR in transduced primary hematopoietic cells[36]. Using live-cell confocal microscopy, we monitored GFP–N-Ras localization in ON cells following treatment with Palm M or ABD957. Consistent with previous studies[7,16], we found that Palm M promoted the time-dependent accumulation of N-Ras at endomembranes that overlapped with the Golgi marker N-acetylgalactosaminyltransferase 2 (GALNT2) (Fig. 4a,b and Supplementary Fig. 3). ABD957, on the other hand, did not cause intracellular accumulation of GFP–N-Ras (Fig. 4a,b), but instead promoted N-Ras retention at the plasma membrane, as reflected in sustained overlapping distribution with the plasma membrane marker protein wheat germ agglutinin (Fig. 4c–e and Supplementary Video 1a–c). The effect of ABD957 was selective for palmitoylated N-Ras, as it was observed in ON, but not ONK cells (Fig. 4c–e). These cell imaging results indicate that ABHD17 inhibition, in addition to partially protecting the palmitoylation state of N-Ras, leads to retention of this protein at the plasma membrane, where ABHD17s are themselves localized[13].

ABD957 blocks NRAS-mutant cancer cell signaling and growth. We next investigated N-Ras signaling, specifically ERK phosphorylation, which we found was substantially blocked by both Palm M and ABD957 in NRAS-mutant OCI-AML3 cells, but not in KRAS mutant NB-4 cells (Fig. 5a,b). By contrast, the MEK inhibitor, PD901, which functions downstream of Ras signaling, blocked ERK phosphorylation in both cell lines (Fig. 5a,b). The effect of Palm M on ERK phosphorylation was greater than ABD957, mirroring their respective impacts on N-Ras palmitoylation (Figs. 2 and 3).

We also found that ABD957 reduced the growth of NRAS-mutant AML cell lines (OCI-AML3, THP1 and HL60), but not KRAS mutant cell lines (NB-4 and NOMO1) (Fig. 5c). The growth inhibitory effects of ABD957 were partial and plateaued at ~500 nM (Fig. 5c) consistent with near-complete inhibition of ABHD17s (Fig. 1f). We next explored the impact of combining ABD957 with PD901 on the growth of ON and ONK cells. Using the Bliss independence model, which assesses drug synergy by comparing observed combination drug responses to predicted combination responses (where predicted responses assume no effect from drug–drug interactions)[37], we found that the combination of ABD957 and PD901 was substantially synergistic in ON cells, but not ONK cells (Fig. 5d and Supplementary Fig. 4). This analysis identifies ABHD17 inhibition as a possible way to augment the therapeutic activity of MEK inhibitors in N-Ras-dependent cancers.

Finally, we generated OCI-AML3 cell lines lacking both ABHD17A and ABHD17B (ABHD17-DKO) or both LYPLA1 and LYPLA2 (LYPLA-DKO) using CRISPR–Cas9 genome editing methods and confirmed selective loss of the knocked-out serine hydrolases in each line by MS-ABPP (Supplementary Fig. 5a and Supplementary Dataset 1). Signals for ABHD17C were low in OCI-AML3 cells, but we did detect a unique peptide for this enzyme, indicating its maintained presence in ABHD17-DKO and LYPLA-DKO cells (Supplementary Fig. 5a and Supplementary Dataset 1). Interestingly, despite not showing an obvious growth defect compared with parental OCI-AML3 or LYPLA-DKO control lines (Supplementary Fig. 5b), ABHD17-DKO cells were insensitive to the antiproliferative effects of ABD957 (Fig. 5e). Additionally, ABD957 no longer suppressed ERK phosphorylation in ABHD17-DKO cells, whereas Palm M maintained similar activity

in these cells compared with control cells (Fig. 5f and Extended Data Fig. 7). Finally, dynamic palmitoylation proteomic experiments revealed that: (1) ABD957-regulated proteins, including N-Ras, were partially protected from depalmitoylation in ABHD17-DKO cells compared with parental OCI-AML3 cells; and (2) the palmitoylation state of ABD957-regulated proteins was no longer sensitive to ABD957 treatment in ABHD17-DKO cells (Extended Data Fig. 8a,b and Supplementary Dataset 3). We interpret these data as strong support that ABD957 produces its effects on protein palmitoylation, N-Ras signaling and cancer growth through inhibiting ABHD17s, with genetic loss of ABHD17A and ABHD17B leading to adaptations in N-Ras mutant AML cells that subvert, by an unknown mechanism, dependency on ABHD17s, while maintaining sensitivity to the more promiscuous depalmitoylation inhibitor Palm M.

Discussion

The fundamental role that C-terminal lipid modifications play in regulating Ras signaling has stimulated efforts to target the post-translational processing of Ras oncoproteins[38–41]. Biochemical and pharmacological studies with first-generation inhibitors of N-Ras depalmitoylation have implicated several enzymes in this process[7], with more recent studies revealing a possible key contribution from the ABHD17 subgroup of serine hydrolases[12]. The high sequence identity shared by ABHD17A, ABHD17B and ABHD17C (>70%) and their co-expression in most cell types present technical challenges for studying the net contribution of these enzymes to N-Ras palmitoylation. Using a pan-ABHD17 inhibitor, ABD957, we have shown here that the ABHD17s make a substantial, but partial contribution to N-Ras depalmitoylation in NRAS-mutant AML cells. Whether other targets of the more promiscuous inhibitor Palm M account for the apparent ABHD17-independent N-Ras depalmitoylation activity remains unknown. We also note that our broader proteomic investigations of Palm M identified several proteins with heightened palmitoylation, including those that were not dynamically palmitoylated over the time course of our pulse–chase experiments. This result suggests that Palm M may affect other cellular metabolic processes beyond protein depalmitoylation that in turn impact the net palmitoylation state of proteins in cells.

One of our most striking findings was the selectivity that ABD957 displayed for N-Ras across the broader palmitoylated proteome. Unlike Palm M, which impacted most dynamically palmitoylated proteins, ABD957 preserved the palmitoylation state of only a handful of plasma membrane-associated proteins. Considering that other dynamically palmitoylated proteins affected by Palm M, but not ABD957, localize to intracellular membrane compartments (Fig. 3d), our data support a model in which ABHD17s regulate palmitoylated proteins mainly at the plasma membrane. Additional factors may influence whether palmitoylated proteins are substrates for ABHD17s, as we noted that transmembrane proteins bearing dynamic palmitoylation events were not affected by ABHD17 inhibition, even when predicted to localize, at least in part, to the plasma membrane (for example, ADAM10, ITM2B/C). We also cannot exclude the possibility that, as more substrates for ABHD17s are identified, some may reside at other locations beyond the plasma membrane in the cell. Conversely, we do not know yet whether individual ABHD17s (A, B or C) show different substrate specificities in cells, but, regardless, it is likely that the substrate scope for these enzymes will expand as more cell types are examined with ABHD17 inhibitors. For instance, PSD-95 (DLG4), a palmitoylated plasma membrane-associated protein that is predominantly expressed in neurons and was not detected in the AML cells examined herein, has also been shown to be regulated by ABHD17s[12,14]. Conversely, SCRIB has been found, in other cell types, to be regulated by the depalmitoylase LYPLA2 (ref. [42]), indicating the potential for cellular context to also restrict the substrate scope of ABHD17s. With regards to enzymes that may be responsible for regulating intracellular protein
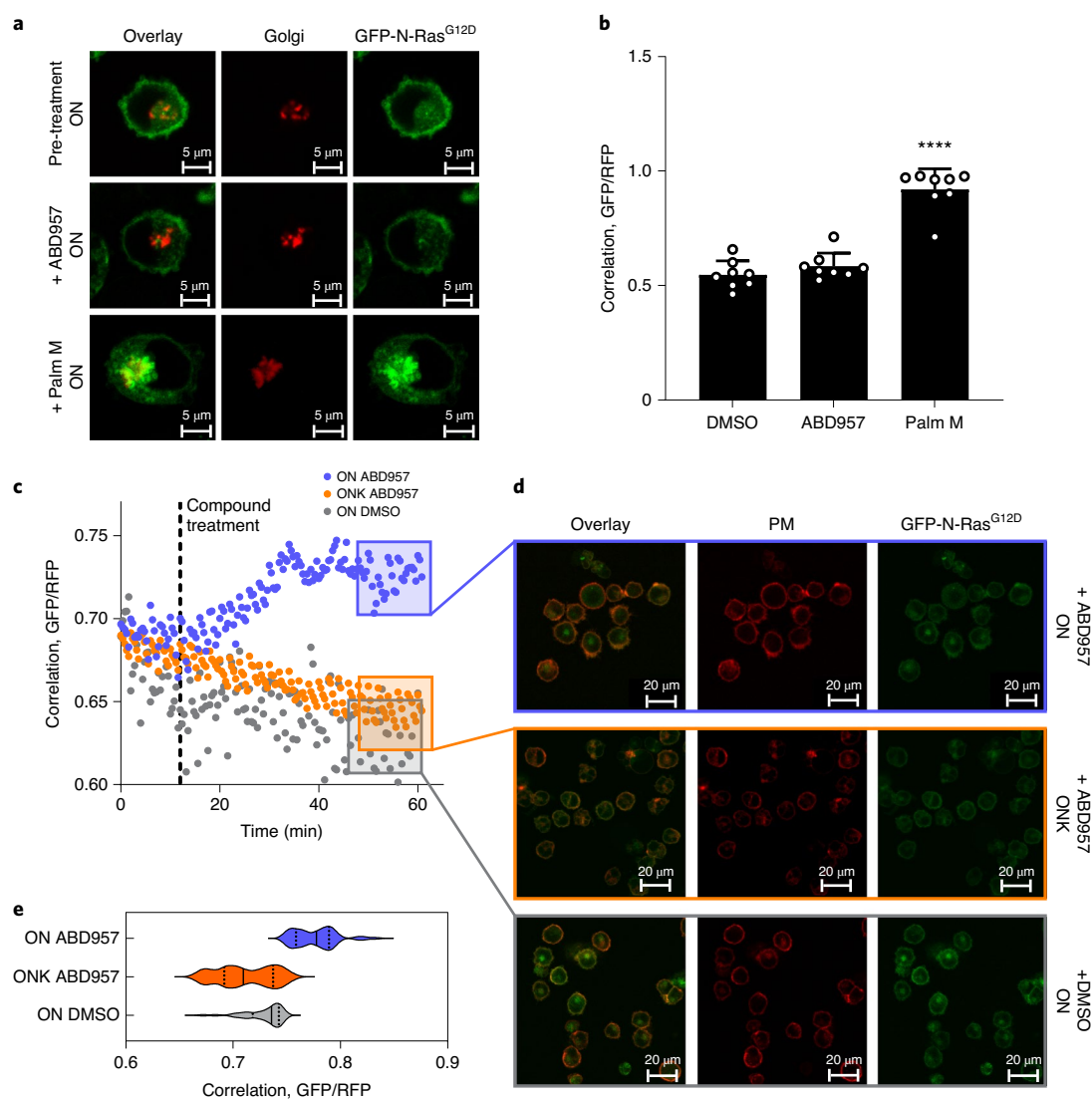
Fig. 4 | Effect of inhibitor treatment on GFP–N-Ras localization in ON and ONK cells. a, Representative images from eight biological replicates of cells co-stained with the Golgi marker red fluorescent protein–*N*-acetylgalactosaminyltransferase (RFP–GALNT2) before and after treatment with Palm M (10 μM) or ABD957 (500 nM). Red channel shows Golgi marker (middle), green channel shows GFP–N-Ras (right) and overlay of the two markers (left). Scale bar, 5 μm. **b**, Change in N-Ras colocalization to the Golgi, as a representative endomembrane compartment, measured by co-staining with RFP–GALNT2 after 10-min compound treatment. Colocalization is quantified using the Mander's correlation coefficient between GFP–N-Ras and RFP–GALNT2 signal. Data represent average values ± s.d. (*n* = 8 individual cells per group). Statistical significance was calculated with unpaired two-tailed Student's *t*-test with equal variance, ****$P < 0.0001$ represents significant increase compared with DMSO. *P* value 1.4×10^{-7}. **c**, Real-time quantification of colocalization of GFP–N-Ras signal intensity and the plasma membrane marker Alexa-647-conjugated wheat germ agglutinin (WGA) in ON (purple) and ONK cells (orange) treated with ABD957 (1 μM at *t* = 10 min) in comparison with ON cells treated with DMSO (gray). Colocalization between GFP and RFP was quantified as in **b** and the correlation coefficient is shown on the *y* axis. Images were acquired every 2 min for 10 min, then medium was infused with ABD957 and images collected for an additional 50 min (see Methods for details). Data shown are representative of three biological replicates. **d**, Representative images taken from **c** at *t* = 60 min (purple, yellow and gray boxes). Red channel shows plasma membrane staining with Alexa-647-conjugated WGA (middle), green channel shows GFP–N-Ras (right) and the overlay of the two markers is also shown (left). Treatment with ABD957 in ON (top) and ONK (middle) or DMSO in ON cells (bottom). Scale bar, 20 μm. **e**, Violin plot of cumulative colocalization between GFP–N-Ras and Alexa-647-conjugated WGA at *t* = 60 min after treatment with ABD957 or DMSO in ON or ONK cells is shown across three biological replicates of time-course experiments as shown in **c**. Median values represented by solid lines, lower and upper quartiles indicated by dotted lines. Also see Supplementary Video 1a–c.

palmitoylation, ABHD10 was recently identified as a depalmitoylase localized to the mitochondria[18], and LYPLA1 localizes to the Golgi[43] and mitochondria[44]. Emerging data thus point to the existence of multiple *S*-depalmitoylases that individually regulate dynamic protein palmitoylation in specific organelles of mammalian cells.

The general strategy of inhibiting the palmitoylation/depalmitoylation cycle of N-Ras has the advantage of selectively targeting cancer cells that depend on this oncoprotein for growth while pre-

serving the functions of K-Ras4b in normal tissues. Our data indicate that ABHD17 inhibitors offer one potential way to achieve this objective. However, several important mechanistic questions about the interactions between ABHD17s and N-Ras palmitoylation and signaling remain to be answered. How, for instance, does ABD957-induced stabilization of palmitoylated N-Ras at the plasma membrane lead to perturbation in N-Ras signaling? Might, for instance, persistently palmitoylated N-Ras mislocalize over time
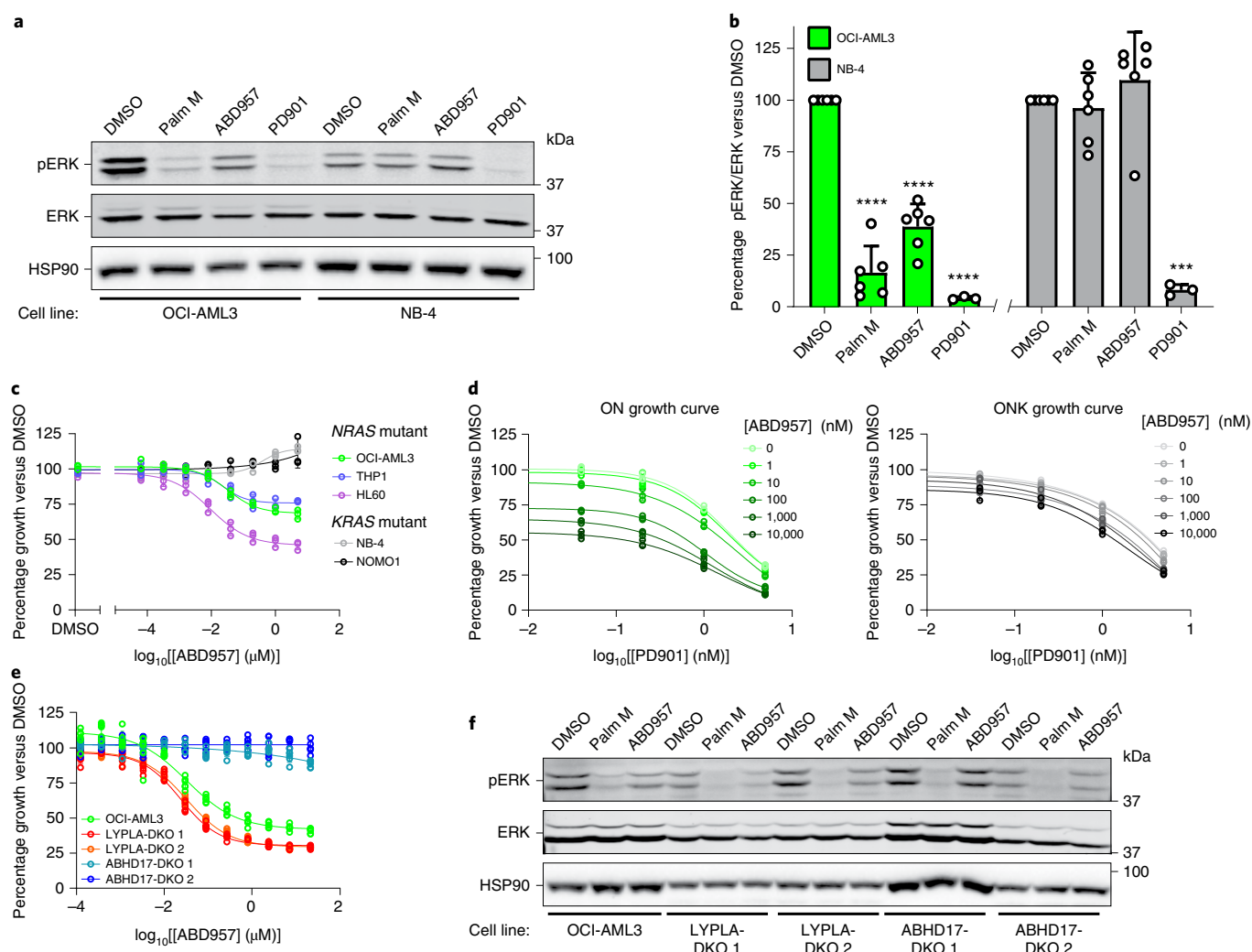
Fig. 5 | ABHD17 inhibition selectively impairs the signaling and proliferation of *NRAS*-mutant leukemia cells. a, Representative western blot for phosphorylated ERK (pERK) following exposure to Palm M (10 μM), ABD957 (500 nM) or PD901 (10 nM) for 4 h in *NRAS*-mutant OCI-AML3 cells or *KRAS* mutant NB-4 cells. **b**, Quantification of data shown in **a**; average values ± s.d. (*n* = 6 independent experiments except for PD901, where *n* = 3 independent experiments). Statistical significance was calculated with unpaired two-tailed Student's *t*-test with unequal variance compared with DMSO control, ***P < 0.001, ****P < 0.0001. P values were 1.9×10⁻⁵ (Palm M OCI-AML3), 3.9×10⁻⁵ (ABD957 OCI-AML3), 2.2×10⁻⁵ (PD901 OCI-AML3) and 0.00028 (PD901 NB-4). **c,d**, Growth of the indicated human AML cell lines (**c**) and of isogenic ON and ONK cells (**d**) treated with varying concentrations of ABD957 for 72 h. Cell growth was measured by CellTiter Glo. Data represent average values ± s.d. (*n* = 3 biological replicates). **e**, Growth of the indicated OCI-AML3 parental and knockout (KO) cell lines treated with varying concentrations of ABD957 for 72 h. Data represent average values ± s.d. (*n* = 6 biological replicates). **f**, Representative western blot measuring pERK effects of compounds in the indicated OCI-AML3 parental and KO cell lines, performed as described in **a**. Quantification of data are shown in Extended Data Fig.7.

to plasma membrane microdomains that are less productive for signal transduction, as has been postulated[45]? Understanding more generally how ABHD17-mediated N-Ras depalmitoylation interfaces with other established modes of regulating N-Ras trafficking and signaling represents another important future direction. For instance, retention of N-Ras in the cytoplasm by chaperones such as PDE6δ and VPS35 (refs. [46,47]) may protect this oncoprotein from depalmitoylation by ABHD17s, and, conversely, the stabilization of N-Ras palmitoylation in ABHD17-inhibited cells may decrease the ability of PDE6δ to extract N-Ras from membranes. We also wonder whether the partial blockade of mutant N-Ras signaling and cancer growth caused by ABHD17 inhibitors reflects maximal possible effects of the plasma membrane-delineated stabilization of mutant N-Ras palmitoylation and if such incomplete activity could facilitate resistance mechanisms, as apparently observed in ABHD17-DKO cells. Considering that Palm M more greatly affected N-Ras

signaling (as measured by ERK phosphorylation), it is possible that disrupting mutant N-Ras signaling on intracellular membranes may be required to more completely block oncogenic activity, an outcome that, based on our data, may not be achievable with ABHD17 inhibition alone. On the other hand, the restricted impact of ABHD17 inhibitors on the palmitoylated proteome suggests that these compounds may perturb N-Ras signaling without gross effects on normal cell physiology. Such a profile may enable ABHD17 inhibitors to safely augment the activity of other anti-cancer agents, as we have shown for the MEK inhibitor PD901, to provide a compelling path for the targeted therapy of *NRAS*-mutant cancers.

Online content

Any methods, additional references, Nature Research reporting summaries, source data, extended data, supplementary information, acknowledgements, peer review information; details of

References

1. Schubbert, S., Shannon, K. & Bollag, G. Hyperactive Ras in developmental disorders and cancer. *Nat. Rev. Cancer* **7**, 295–308 (2007).
2. Ostrem, J. M., Peters, U., Sos, M. L., Wells, J. A. & Shokat, K. M. K-Ras(G12C) inhibitors allosterically control GTP affinity and effector interactions. *Nature* **503**, 548–551 (2013).
3. Canon, J. et al. The clinical KRAS(G12C) inhibitor AMG 510 drives anti-tumour immunity. *Nature* **575**, 217–223 (2019).
4. Omerovic, J., Laude, A. J. & Prior, I. A. Ras proteins: paradigms for compartmentalised and isoform-specific signalling. *Cell. Mol. Life Sci.* **64**, 2575–2589 (2007).
5. Hancock, J. F., Paterson, H. & Marshall, C. J. A polybasic domain or palmitoylation is required in addition to the CAAX motif to localize p21^{ras} to the plasma membrane. *Cell* **63**, 133–139 (1990).
6. Rocks, O. et al. An acylation cycle regulates localization and activity of palmitoylated Ras isoforms. *Science* **307**, 1746–1752 (2005).
7. Dekker, F. J. et al. Small-molecule inhibition of APT1 affects Ras localization and signaling. *Nat. Chem. Biol.* **6**, 449–456 (2010).
8. Hedberg, C. et al. Development of highly potent inhibitors of the Ras-targeting human acyl protein thioesterases based on substrate similarity design. *Angew. Chem. Int. Ed. Engl.* **50**, 9832–9837 (2011).
9. Martin, B. R., Wang, C., Adibekian, A., Tully, S. E. & Cravatt, B. F. Global profiling of dynamic protein palmitoylation. *Nat. Methods* **9**, 84–89 (2011).
10. Duncan, J. A. & Gilman, A. G. A cytoplasmic acyl-protein thioesterase that removes palmitate from G protein alpha subunits and p21(RAS). *J. Biol. Chem.* **273**, 15830–15837 (1998).
11. Rusch, M. et al. Identification of acyl protein thioesterases 1 and 2 as the cellular targets of the Ras-signaling modulators palmostatin B and M. *Angew. Chem. Int. Ed. Engl.* **50**, 9838–9842 (2011).
12. Lin, D. T. & Conibear, E. ABHD17 proteins are novel protein depalmitoylases that regulate N-Ras palmitate turnover and subcellular localization. *eLife* **4**, e11306 (2015).
13. Martin, B. R. & Cravatt, B. F. Large-scale profiling of protein palmitoylation in mammalian cells. *Nat. Methods* **6**, 135–138 (2009).
14. Yokoi, N. et al. Identification of PSD-95 depalmitoylating enzymes. *J. Neurosci.* **36**, 6431–6444 (2016).
15. Jia, L. et al. A mechanism regulating G protein-coupled receptor signaling that requires cycles of protein palmitoylation and depalmitoylation. *J. Biol. Chem.* **289**, 6249–6257 (2014).
16. Won, S. J. & Martin, B. R. Temporal profiling establishes a dynamic S-palmitoylation cycle. *ACS Chem. Biol.* **13**, 1560–1568 (2018).
17. Zhang, M. M., Tsou, L. K., Charron, G., Raghavan, A. S. & Hang, H. C. Tandem fluorescence imaging of dynamic S-acylation and protein turnover. *Proc. Natl Acad. Sci. USA* **107**, 8627–8632 (2010).
18. Cao, Y. et al. ABHD10 is an S-depalmitoylase affecting redox homeostasis through peroxiredoxin-5. *Nat. Chem. Biol.* **15**, 1232–1240 (2019).
19. Adibekian, A. et al. Click-generated triazole ureas as ultrapotent in vivo-active serine hydrolase inhibitors. *Nat. Chem. Biol.* **7**, 469–478 (2011).
20. Chang, J. W., Nomura, D. K. & Cravatt, B. F. A potent and selective inhibitor of KIAA1363/AADACL1 that impairs prostate cancer pathogenesis. *Chem. Biol.* **18**, 476–484 (2011).
21. Hsu, K. L. et al. DAGLbeta inhibition perturbs a lipid network involved in macrophage inflammatory responses. *Nat. Chem. Biol.* **8**, 999–1007 (2012).
22. Niphakis, M. J. & Cravatt, B. F. Enzyme inhibitor discovery by activity-based protein profiling. *Annu. Rev. Biochem.* **83**, 341–377 (2014).
23. Otrubova, K., Chatterjee, S., Ghimire, S., Cravatt, B. F. & Boger, D. L. N-Acyl pyrazoles: effective and tunable inhibitors of serine hydrolases. *Bioorg. Med. Chem.* **27**, 1693–1703 (2019).
24. Liu, Y., Patricelli, M. P. & Cravatt, B. F. Activity-based protein profiling: the serine hydrolases. *Proc. Natl Acad. Sci. USA* **96**, 14694–14699 (1999).
25. Cognetta, A. B. 3rd et al. Selective N-hydroxyhydantoin carbamate inhibitors of mammalian serine hydrolases. *Chem. Biol.* **22**, 928–937 (2015).
26. Zambetti, N. A. et al. Genetic disruption of N-RasG12D palmitoylation perturbs hematopoiesis and prevents myeloid transformation in mice. *Blood* **135**, 1772–1782 (2020).
27. Charron, G. et al. Robust fluorescent detection of protein fatty-acylation with chemical reporters. *J. Am. Chem. Soc.* **131**, 4967–4975 (2009).
28. Rostovtsev, V. V., Green, L. G., Fokin, V. V. & Sharpless, K. B. A stepwise huisgen cycloaddition process: copper(I)-catalyzed regioselective 'ligation' of azides and terminal alkynes. *Angew. Chem. Int. Ed. Engl.* **41**, 2596–2599 (2002).
29. Drisdel, R. C. & Green, W. N. Labeling and quantifying sites of protein palmitoylation. *Biotechniques* **36**, 276–285 (2004).
30. Zecha, J. et al. Peptide level turnover measurements enable the study of proteoform dynamics. *Mol. Cell. Proteomics* **17**, 974–992 (2018).
31. Chen, B. et al. ZDHHC7-mediated S-palmitoylation of scribble regulates cell polarity. *Nat. Chem. Biol.* **12**, 686–693 (2016).
32. Kamijo, A., Saitoh, Y., Ohno, N., Ohno, S. & Terada, N. Immunohistochemical study of the membrane skeletal protein, membrane protein palmitoylated 6 (MPP6), in the mouse small intestine. *Histochem. Cell Biol.* **145**, 81–92 (2016).
33. Jones, T. L. & Gutkind, J. S. Galpha12 requires acylation for its transforming activity. *Biochemistry* **37**, 3196–3202 (1998).
34. Saraceno, C. et al. SAP97-mediated ADAM10 trafficking from Golgi outposts depends on PKC phosphorylation. *Cell Death Dis.* **5**, e1547 (2014).
35. Choi, S. I., Vidal, R., Frangione, B. & Levy, E. Axonal transport of British and Danish amyloid peptides via secretory vesicles. *FASEB J.* **18**, 373–375 (2004).
36. Xu, J. et al. Inhibiting the palmitoylation/depalmitoylation cycle selectively reduces the growth of hematopoietic cells expressing oncogenic Nras. *Blood* **119**, 1032–1035 (2012).
37. Zhao, W. et al. A new bliss independence model to analyze drug combination data. *J. Biomol. Screen.* **19**, 817–821 (2014).
38. Ahearn, I. M., Haigis, K., Bar-Sagi, D. & Philips, M. R. Regulating the regulator: post-translational modification of RAS. *Nat. Rev. Mol. Cell Biol.* **13**, 39–51 (2011).
39. Ryan, M. B. & Corcoran, R. B. Therapeutic strategies to target RAS-mutant cancers. *Nat. Rev. Clin. Oncol.* **15**, 709–720 (2018).
40. Cox, A. D., Der, C. J. & Philips, M. R. Targeting RAS membrane association: back to the future for anti-RAS drug discovery? *Clin. Cancer Res.* **21**, 1819–1827 (2015).
41. Cox, A. D., Fesik, S. W., Kimmelman, A. C., Luo, J. & Der, C. J. Drugging the undruggable RAS: mission possible? *Nat. Rev. Drug Discov.* **13**, 828–851 (2014).
42. Hernandez, J. L. et al. APT2 inhibition restores scribble localization and S-palmitoylation in Snail-transformed cells. *Cell Chem. Biol.* **24**, 87–97 (2017).
43. Vartak, N. et al. The autodepalmitoylating activity of APT maintains the spatial organization of palmitoylated membrane proteins. *Biophys. J.* **106**, 93–105 (2014).
44. Kathayat, R. S. et al. Active and dynamic mitochondrial S-depalmitoylation revealed by targeted fluorescent probes. *Nat. Commun.* **9**, 334 (2018).
45. Levental, I., Lingwood, D., Grzybek, M., Coskun, U. & Simons, K. Palmitoylation regulates raft affinity for the majority of integral raft proteins. *Proc. Natl Acad. Sci. USA* **107**, 22050–22054 (2010).
46. Chandra, A. et al. The GDI-like solubilizing factor PDEdelta sustains the spatial organization and signalling of Ras family proteins. *Nat. Cell Biol.* **14**, 148–158 (2011).
47. Zhou, M. et al. VPS35 binds farnesylated N-Ras in the cytosol to regulate N-Ras trafficking. *J. Cell Biol.* **214**, 445–458 (2016).
48. Nakai, K. & Horton, P. PSORT: a program for detecting sorting signals in proteins and predicting their subcellular localization. *Trends Biochem. Sci.* **24**, 34–36 (1999).

Methods

Cell lines and tissue culture. OCI-AML3 (DSMZ, ACC-582) cells were grown in RPMI supplemented with 10% fetal bovine serum (FBS), L-glutamine (2 mM), penicillin (100 U ml^{-1}), streptomycin (100 µg ml^{-1}) and 50 µM β-mercaptoethanol, and grown at densities between 0.3×10^6 and 2×10^6 cells ml^{-1}. NB-4 (DSMZ, ACC-207), NOMO1 (DSMZ, ACC-542), HL60 (DSMZ, ACC-3) and THP1 (ATCC, TIB-202) were grown in RPMI, HEK293T (ATCC, CRL-3216) were grown in DMEM and PC3 (ATCC, CRL-1435) were grown in F-12K, all supplemented with 10% FBS, L-glutamine (2 mM), penicillin (100 U ml^{-1}) and streptomycin (100 µg ml^{-1}). All cells were maintained at 37 °C with 5% CO$_2$.

hABHD17B (MHS1010-202726047, 4748883) and mABHD13 (MMM1013-202768782, 5148187) clones in pCMD-SPORT6 vector were purchased from GE Dharmacon (now known as Dharmacon Inc).

hCES2 in pcDNA3.1 vector was a custom order from GenScript.

The following primers were used for subcloning into an untagged pCL vector for viral transfection: 5′-TTTAAGCTTGCCACCATGAATAATCTTTCATTTA GTG-3′ (forward; FAM108B1_F_pCL_HindIII), 5′-AAACTCGAGTTACAA ATTTACCAGTTCCTG-3′ (reverse; FAM108B1_R_pCL_XhoI).

Generation of HEK293T transgenic lines. HEK293T cells stably expressing various constructs were made as follows. HEK293T cells (1.8×10^6) were plated in 6-cm plates and allowed to settle overnight. To 200 µl of serum-free DMEM the following were added: 1 µg of plasmid containing the gene of interest in lentivirus vector, 900 ng of ΔVPR, 100 ng of VSV-G and 6 µl of XtremeGene HP transfection reagent. Reagents were flicked to mix, and after 15 min, the transfection mixture was added dropwise to plates containing cells. Virus-containing supernatants were collected 48 h later and concentrated using a Lenti-X Concentrator (Clontech), and then used to infect HEK293T cells (plated the day before at 0.25×10^6 per well of 12-well plate) in the presence of 10 µg ml^{-1} Polybrene (Santa Cruz). The media was replaced 24 h later, cells were allowed to recover for an additional 24 h, and then puromycin was added for selection.

Gel-based activity-based protein profiling. Inhibitor potency (IC$_{50}$ values) against hABHD17B, hLYPLA1, mABHD13 and hABHD6 was determined by competitive gel-based ABPP using FP-Rhodamine (FP-Rh)[49] (hABHD17B, hLYPLA1 and mABHD13) or JW912 (ref. [50]) (hABHD6) competition. Endogenous hLYPLA1 and hABHD6 activity was measured in HEK293T and PC3 proteomes, respectively, whereas hABHD17B and mABHD13 activity was measured in HEK293T cell proteomes overexpressing this protein (see above).

Cell lysates were fractionated by ultra-centrifugation (100,000g for 45 min at 4 °C) and membrane pellets were resuspended in PBS and diluted to a final protein concentration of 1.0 mg ml^{-1} for HEK293T or 2.0 mg ml^{-1} for PC3. Cell proteomes (50 µg) were treated with inhibitor (0.001–10 µM) or DMSO for 30 min at 37 °C and subsequently treated with FP-Rh or JW912 (1.0 µM) for an additional 30 min at room temperature. Reactions were quenched with 4× SDS–PAGE loading buffer and FP-Rh-labeled enzymes were resolved by SDS–PAGE (10% acrylamide). In-gel fluorescence was visualized using a Bio-Rad ChemiDoc XRS imager. Fluorescence is shown in gray scale. Quantification of enzyme activities was performed by densitometric analysis using ImageJ software (NIH). Integrated peak intensities were generated for bands corresponding to hABHD17B, hLYPLA1, mABHD13 and hABHD6. IC$_{50}$ values were calculated through curve fitting semi-log-transformed data (x axis) by nonlinear regression with the log(inhibitor) versus normalized response function in Prism software (GraphPad).

In vitro competitive substrate hydrolysis activity assay for hCES2. Inhibitor potency (IC$_{50}$ values) against hCES2 was determined by measuring the rate of enzyme hydrolysis of the substrate 4-nitrophenyl acetate (pNPA) (Sigma, catalog no. N8130; CAS, 830-03-5) based on a previously described method[51].

HEK293T cell lysates expressing recombinant hCES2 and pNPA substrate were diluted separately in 50 mM HEPES (pH 7.0) containing 100 mM NaCl. Lysates (50 µl, ~2.5 µg total protein) were preincubated with varying concentrations of inhibitors (0.03–2 µM) or DMSO for 30 min at 25 °C. Subsequently, 2× pNPA substrate (50 µl, 2.5 mM) was added and the rate of substrate turnover was monitored by measuring the increase in absorbance at 405 nm for 20 min at 25 °C using a BioTek Neo2 plate reader. Mean velocity was converted to percent enzyme activity following background subtraction of nonspecific substrate turnover and normalization to DMSO controls. The mean reaction velocity (V_{mean}, ΔAbs min^{-1} µg protein^{-1}) in mock-transfected versus hCES2-transfected proteomes was 8.72 ± 1.86 and 30.9 ± 1.16 min^{-1} µg^{-1}, respectively. IC$_{50}$ values were calculated through curve fitting semi-log-transformed data (x axis) by nonlinear regression with the log(inhibitor) versus normalized response function in Prism software (GraphPad).

Liver microsomal stability. A master solution was first prepared by mixing pooled human liver microsomes (50 µl, 5 mg ml^{-1}; Corning, catalog no. 452117), phosphate buffer (250 µl, 200 mM), ultrapure water (95 µl) and MgCl$_2$ solution (50 µl, 50 mM). A solution of NADPH (50 µl, 10 mM) or ultrapure water (50 µl, negative control) was then added to the master solution and the mixture was warmed to 37 °C for 5 min. To begin the reaction, test compounds (5 µl, 200 µM) were then added to the

mixture ($t = 0$). Aliquots (50 µl) were removed from the reaction solution at 0, 15, 30, 45 and 60 min, and immediately quenched with acetonitrile (200 µl), diluted with ultrapure water (90 µl) and analyzed by liquid chromatography tandem mass spectrometry (LC/MS/MS). Extracted ion chromatograms were integrated and peak areas were plotted against the incubation time to determine in vitro $t_{1/2}$. Intrinsic clearance (Cl$_{int}$) was calculated using the following equation:

$$\text{in vitro Cl}_{\text{int}} = \left(\frac{0.693}{t_{1/2}} \right) \left(\frac{\text{incubation volume, } \mu l}{\text{total microsomal protein, } mg} \right)$$

MS-ABPP sample preparation. For in situ treatments, OCI-AML3 or ONK cells were resuspended in fresh media at 2×10^6 cells ml^{-1} and treated with DMSO, Palm M (10 µM), HDFP (20 µM), JJH254 (1 µM), ABD298 (500 nM) or ABD957 (500 nM or 1 µM) and incubated for the indicated times. Cells were pelleted at 500g by centrifugation, washed with PBS, pelleted again and snap frozen.

Frozen cell pellets were thawed, diluted in PBS and subsequently lysed by probe sonication. The membrane fraction of each cell sample was isolated using ultra-centrifugation (100,000g for 45 min at 4 °C) and membrane pellets were resuspended in PBS and diluted to 2.0 mg ml^{-1}. Membrane proteomes (2 mg ml^{-1} in 1 ml of PBS) were labeled with FP-biotin (10 µM) for 1 h at room temperature while rotating. After labeling, the proteomes were denatured and precipitated using 4:1 MeOH/CHCl$_3$, resuspended in 0.5 ml of 6 M urea in PBS, reduced using tris(2-carboxyethyl)phosphine (TCEP, 10 mM) for 30 min at 37 °C, and then alkylated with iodoacetamide (40 mM) for 30 min at room temperature in the dark. The biotinylated proteins were enriched with PBS-washed avidin–agarose beads (100 µl; Sigma-Aldrich) by rotating at room temperature for 1.5 h in PBS with 0.2% SDS (6 ml). The beads were then washed sequentially with 5 ml of 0.2% SDS in PBS (3×), 5 ml of PBS (3×) and 5 ml of H$_2$O (3×). On-bead digestion was performed using sequencing-grade trypsin (2 µg; Promega) in 2 M urea in 100 mM triethylammonium bicarbonate buffer with 2 mM CaCl$_2$ for 12–14 h at 37 °C (200 µl).

Samples from the time-course study with compound **7** and ABD957 were desalted using SOLAµ SPE plates (Hydrophobic Reversed Phase 2 mg per 1 ml), dried by centrifugal evaporation and stored at −80 °C until analysis by parallel reaction monitoring.

For all other samples, duplex reductive dimethylation was performed as previously described[52]. Briefly, for duplex reductive dimethylation of wild type (WT) versus knockout (KO) (or DMSO versus inhibitor-treated) cells either ^{13}CD$_2$O (heavy) or CH$_2$O (light) was added to each sample (0.15%) followed by addition of NaBH$_3$CN (22.2 mM). Following a 1-h incubation period at room temperature, the reaction was quenched by addition of NH$_4$OH (0.23%) and formic acid (0.5%). The samples were then combined, desalted using SOLAµ SPE plates (HRP 2 mg per 1 ml) and dried by centrifugal evaporation and stored at −80 °C until analysis using data-dependent acquisition LC/MS/MS methods.

MS-ABPP data analysis. *Data-dependent acquisition.* Nanoflow LC/MS/MS measurements were performed on a Dionex RSLC nano-LC (Thermo Fisher Scientific) interfaced with an Orbitrap Fusion Lumos Tribrid mass spectrometer (Thermo Fisher Scientific) via an EASY-Spray source (Thermo Fisher Scientific). Data were collected using Xcalibur (v.2.2). Dry peptide samples were reconstituted in a water/acetonitrile (95:5) mixture containing 0.1% formic acid (30 µl) and 20 µl were injected on an EASY-Spray C18 column (2 µm particle size; 75 µm × 50 cm; Thermo Fisher Scientific, ES801) heated to 55 °C using a flow rate of 400 nl min^{-1}. The compositions of LC solvents were: A, water and 0.1% formic acid; and B, 95% acetonitrile, 5% water and 0.1% formic acid. Peptides were eluted over 4 h using the linear gradient: 2.5–215 min, 3–35% B; 215–230 min, 25–40% B; 230–231 min, 45–70% B; 231–233 min, 70–90% B; 233–234 min, 5–70% B; 234–236 min, 70–90% B; and 236–240 min, 3% B.

MS data were acquired in data-dependent mode (top 20 dependent scans). MS1 profile scans were acquired in the Orbitrap (resolution, 120,000; scan range, 375–1,500 m/z; AGC target, 4.0×10^5; maximum injection time, 50 ms). Monoisotopic peak determination was set to 'peptide'. Only charge states 2–5 were included. Dynamic exclusion was enabled (repeat count; n, 1; exclusion duration, 60 s; mass tolerance, ppm; low, 10 and high, 10; excluding isotopes). An intensity threshold of 5×10^3 was set. MS2 spectra were acquired in centroid mode. Precursor ions were isolated using the quadrupole (isolation window, 1.6 m/z), fragmented using collision-induced dissociation (collision energy, 35%; activation time, 10 ms; activation Q, 0.25), and detected in the ion trap (scan range mode, auto m/z normal; scan rate, rapid; AGC target, 4.0×10^3; maximum injection time, 300 ms; injecting ions for all available parallelizable time).

Spectrum raw files were extracted into MS2 files using RawConverter (v.1.1.0.22 from http://fields.scripps.edu/rawconv/) and searched using the ProLuCID (v.1.4) algorithm[53] against a human reverse concatenated nonredundant UniProt database (2016 version), with static modifications for cysteine residues to account for alkylation by iodoacetamide (+57.0215 m/z), and standard static modifications for reductive dimethylation: lysine and N terminus (+28.0313 m/z for light, +34.06312 m/z for heavy). Data were assembled using DTASelect v.2.0 (ref. [54]), and ratio quantification was performed using in-house CIMAGE software (see GitHub repository linked in Data Availability section). Peptides were required

to be fully tryptic, unique, to have a peak-pair coelution score of $R^2 \geq 0.5$, and ratios were capped to a maximum value of 20. Ratios (R) for each protein were calculated from the median of all quantified peptide ratios. In cases where a protein had exactly one peptide with a ratio of 20, and at least one other peptide with a ratio below 2, the 20 value was discarded. Peptides with a ratio of 20 were also manually reviewed and filtered.

For in vitro datasets ($n=1$), peptides with ratios of 20 and only a single MS2 event triggered during elution of the parent ion were discarded. Proteins were required to have at least two quantified peptides.

For in situ datasets ($n=3$), peptides with ratios of 20 and only a single MS2 event triggered during elution of the parent ion were discarded. Proteins were required to be quantified in at least two biological replicates, and to have at least two unique quantified peptides across all replicates. Additionally, for proteins with $R=20$ in one experimental replicate and $R \leq 2$ in one or more replicates, the 20 value was discarded. The median ratio was calculated and reported across experimental replicates.

For CRISPR knockout datasets ($n=1$), chromatograms showing evidence of knockdown were manually selected.

Parallel reaction monitoring. Dry peptide samples were reconstituted in a water/acetonitrile (95:5) mixture containing 0.1% formic acid (30 μl) and 5 μl was injected on to an EASY-Spray C18 column (2 μm particle size, 75 μm × 50 cm; Thermo Fisher Scientific, ES801) using a Dionex RSLC nano-LC (Thermo Fisher Scientific). Peptides were separated over a 60-min gradient of 0 to 40% acetonitrile (0.1% formic acid) and analyzed on an Orbitrap Fusion Lumos (Thermo Fisher Scientific) operated using a parallel reaction monitoring method for two distinct peptides for each serine hydrolase (ABHD17A, ABHD17B, ABHD17C, LYPLA1, LYPLA2) and ten additional peptides from endogenously biotinylated proteins (PCCA and MCCC1) as controls. Selected ions were isolated and fragmented by high-energy collision dissociation and fragments were detected in the Orbitrap at 15,000 resolution. Peptide sequences and targeting parameters can be found in Supplementary Table 3.

Raw data files were uploaded analyzed in Skyline (v.4.2.0.19009) to determine the abundance of each peptide in vehicle-treated samples relative to inhibitor-treated samples. Peptide quantification was performed by calculating the sum of the peak areas corresponding to six fragment ions from each peptide. The peptides and fragment ions were preselected from in-house reference spectral libraries acquired in data-dependent acquisition mode to identify authentic spectra for each peptide.

Syngeneic ON/ONK cells. A pCDH-LMN–GFP lentiviral vector was obtained by cloning the miR30-PGK-NeoR-IRES–GFP cassette from LMN–GFP[55] into a pCDH Expression Lentivector (System Biosciences). A miR30-based shRNA targeting human *NRAS* (sense, 5′-CAGGGTGTTGAAGATGCTTTT-3′) was cloned into the vector. The coding sequence of *Nras^G12D* was cloned downstream of GFP to create a N-terminal GFP-fused N-Ras^G12D expression construct with N-Ras endogenous HVR (N-HVR). Alternatively, a chimeric version was cloned where the sequence corresponding to amino acids 166–188 from N-Ras was replaced with that of K-Ras4b (K-HVR). Lentiviral vector production and transduction of OCI-AML3 cells were performed as previously described[56]. ON and ONK cells were validated by western blot (Supplementary Fig. 1).

Dynamic palmitoylation assay. Dynamic palmitoylation assay was modeled after earlier work in our laboratory[9]. OCI-AML3 cells were grown as described above, then spun down (3 min, 500*g*) and resuspended in fresh medium at a density of 2×10^6 cells ml^{-1} (10×10^6 cells per sample for gel-based assay and 20×10^6 cells per sample for MS-based assay). Cells were preincubated with inhibitor or DMSO for 1 h, then 17-ODYA (20 μM) was added for 1 h. Samples were pelleted and snap frozen immediately following the 17-ODYA 'pulse' and designated t_0, or resuspended in pre-warmed chase medium which consisted of OCI-AML3 growth media, supplemented with DMSO or inhibitor at the same concentration as in the preincubation step and incubated for 1 h. Cells were then centrifuged, placed on ice, washed in cold PBS, snap frozen and designated t_1.

Immunoprecipitation. Cell pellets were resuspended in cold lysis buffer which consisted of 1% Triton-X PBS with 1 mM phenylmethyl sulfonyl fluoride (PMSF), 0.2 mM hexadecyl sulfonyl fluoride (HDSF), 20 μM HDFP and protease inhibitors (complete Ultra EDTA-free mini tablets, 5892791001 Roche), sonicated with a microtip probe sonicator (seven times, 50% rate, power 4), and placed on an end-over-end rotator for 30 min at 4 °C. Samples were then hard spun (16,300*g*, 5 min) and the supernatant was transferred to fresh tubes on ice. Protein concentration was measured using a detergent compatible (DC) assay kit from Bio-Rad and adjusted to 1 mg ml^{-1}. Input samples were taken at this point and stored at −80 °C.

Enrichment was performed with anti-GFP Sepharose beads (20 μl of 50:50 slurry, ab69314, Abcam). Antibody conjugated beads were spun down (500*g*), storage buffer was aspirated with a 26-gauge needle, and beads were washed three times with 1% Triton-X PBS. To each sample, 20 μl of washed bead slurry was added using a cut pipette tip, and samples were placed on an end-over-end rotator

for 3 h at 4 °C. Next, washes were performed by centrifugation/aspiration (3×, 500*g*) with cold 1% Triton-X PBS containing 500 mM NaCl. After the last wash, supernatant was removed, and a 26-gauge needle was quickly inserted into the bead slurry to remove all remaining liquid. GFP beads were then resuspended in 50 μl of wash buffer. At this point, immunoprecipation samples were either stored at −80 °C or processed further for analysis by SDS–PAGE gel.

Click chemistry and processing for SDS–PAGE gel. On-bead click chemistry was performed to conjugate a rhodamine fluorophore reporter to 17-ODYA labeled proteins. To each 50-μl sample, 6 μl of a click chemistry reaction mixture was added. The click reaction mixture was freshly prepared as follows (amounts given are per sample): 1 μl of 50 mM CuSO$_4$ (in water; final concentration during reaction of 1 mM), 3 μl of 1.7 mM tris(benzyltriazolylmethyl)amine (4:1 *t*-BuOH/DMSO; 100 μM final), 1 μl of 50 mM TCEP (freshly made in PBS; 1 mM final) and 1 μl of Rh-N$_3$ (DMSO; 25 μM final). Reactions were allowed to proceed for 1 h at room temperature. Samples were then quenched with 4× SDS loading buffer containing 1% β-mercaptoethanol (described below), boiled for 5 min to effect elution and finally 17-ODYA proteins were resolved and imaged on gel.

Loading buffer was prepared as follows (for 100 ml): 3.02 g of Tris base was added to 40 ml of water, 40 ml of glycerol was added slowly and the mixture was stirred using a stir bar while the pH was brought to 6.75 using concentrated HCl; 8 g of SDS were then added followed by 20 ml of water and a pinch of bromophenol blue. Loading buffer was stored at room temperature, and 1% (10 μl per 1 ml of buffer) β-mercaptoethanol was added immediately before quenching.

Finally, samples were loaded on to a 10% acrylamide gel, resolved by SDS–PAGE (300 V for ~2.5 h), and in-gel fluorescence was visualized using a Bio-Rad ChemiDoc MP flatbed fluorescence scanner.

Preparation of TMT-labeled 17-ODYA enrichment samples. Samples were prepared as previously described[9], with the following modifications. 17-ODYA-labeled cells were lysed in Dulbecco's phosphate-buffered saline (DPBS) containing protease inhibitors (Roche) and 1 mM PMSF using a Branson Sonifier probe sonicator (three rounds of eight pulses, 40% duty cycle, output setting = 4). Protein concentration was determined by DC assay on a microplate reader, and 500 μl of whole-cell lysate at 2 mg ml^{-1} was added to a mixture of tris(benzyltriazolylmethyl)amine (30 μl per sample, 1.7 mM in 1:4 DMSO/*t*-BuOH), CuSO$_4$ (10 μl per sample, 50 mM in H$_2$O), TCEP (10 μl per sample, 50 mM in DPBS) and biotin-N$_3$ (10 μl per sample, 10 mM in DMSO). After 1 h, samples were MeOH/CHCl$_3$ precipitated. Hydroxylamine-sensitivity was performed as previously described for cells metabolically labeled with 17-ODYA for 2 h (ref. [9]). Following precipitation, each sample was solubilized in 1.2% SDS in DPBS via sonication and diluted to 0.2% SDS for enrichment. Streptavidin beads (Thermo Fisher Scientific) in 100 μl of slurry were added to each sample and rotated at room temperature for 2 h, washed three times with 0.2% SDS, three times with DPBS and three times with water. Beads were resuspended in 6 M urea in 200 mM 3-[4-(2-Hydroxyethyl)piperazin-1-yl]propane-1-sulfonic acid (EPPS), reduced with 10 mM neutral TCEP for 30 min at 37 °C followed by addition of 20 mM iodoacetamide for 30 min at room temperature. Samples were diluted to 2 M urea in 200 mM EPPS, pelleted and resuspended with 200 μl of 2 M urea in 200 mM EPPS containing 2 μg sequence grade porcine trypsin (Promega) and 1 mM CaCl$_2$ and digested overnight at 37 °C. Digests were centrifuged to remove the beads, and acetonitrile was added to reach 30% final volume. Six microliters (20 μg μl^{-1}) of respective 6-plex, 10-plex or 16-plex TMT tag (Thermo Fisher Scientific) was added to digests and incubated at room temperature for 1 h with occasional vortexing. Labeling reaction was quenched with 6 μl of 5% hydroxylamine for 15 min, followed by acidification with 15 μl of formic acid. Samples were combined and vacuum-centrifuged to dryness to remove acetonitrile, reconstituted in buffer A (95% H$_2$O, 5% acetonitrile, 0.1% formic acid) and stored at −80 °C until MS analysis by Multidimensional Protein Identification Technology (MudPIT) or offline fractionated using Pierce High pH Reversed-Phase Peptide Fractionation Kit (Thermo Fisher Scientific), separating samples into nine fractions concatenated into three.

Mass spectrometry analysis of TMT-labeled peptides. Labeled peptides were prepared for MS analysis as previously described[57]. Briefly, labeled peptides were pressure loaded on to a 250 μm (inner diameter) fused silica capillary column packed with 4 cm of C18 resin (Phenomenex, Aqua 5 μm). Samples were analyzed on an Orbitrap Fusion mass spectrometer (Thermo Fisher Scientific) coupled to an UltiMate 3000 Series Rapid Separation LC system and autosampler (Dionex; Thermo Fisher Scientific). Data were collected using Xcalibur (v.2.2). Peptides were either separated on a 100-μm inner diameter capillary column with a 5-μm tip packed with 10 cm of C18 (Phenomenex, Aqua 5 μm) and 3 cm of strong cation exchange resin (Phenomenex) using a five-step MudPIT protocol that injects 5 μl of 0%, 20%, 50%, 80% and 100% salt bumps of ammonium acetate (500 mM) in buffer A (100% H$_2$O, 0.1% formic acid) followed by an increasing gradient of buffer B (100% acetonitrile, 0.1% formic acid) in buffer A in each step, or the peptides were eluted on to a capillary column (75 μm inner diameter fused silica, packed with C18; Waters, Acquity BEH C18, 1.7 μm, 25 cm) and separated at a flow rate of 0.25 μl min^{-1} using the following gradient: 5% buffer B in buffer A from 0 to

15 min, 5–35% buffer B from 15 to 155 min, 35–95% buffer B from 155 to 160 min, 95% buffer B from 160 to 169 min, 95% to 5% buffer B from 169 to 170 min and 5% buffer B from 170 to 200 min (buffer A: 95% H_2O, 5% acetonitrile, 0.1% formic acid; buffer B: 5% H_2O, 95% acetonitrile, 0.1% formic acid). The voltage applied to the nano-LC electrospray ionization source was 1.9 kV. A MS3-based TMT method was used for data acquisition. MS1 full-scan spectrum (resolution, 120,000; scan range, 400–1,700 m/z; RF lens 60%; AGC target, 2×10^5; maximum injection time, 50 ms; centroid mode) with dynamic exclusion enabled (repeat count 1, duration 15 s) was performed. The top ten precursors were then selected for MS2/MS3 analysis. MS2 analysis consisted of quadrupole ion trap analysis, AGC 1.8×10^4, collision-induced dissociation energy 35%, Activation Q 0.25, maximum injection time 120 ms, and isolation window at 0.7 m/z. Synchronous precursor selection was enabled to include up to ten MS2 fragment ions for the MS3 spectrum. MS3 precursors were fragmented by high-energy collision dissociation and analyzed using the Orbitrap (resolution, 15,000 for 6-plex and 50,000 for 10-plex and 16-plex; collision energy, 55%; AGC, 1.5×10^5; maximum injection time, 120 ms). For MS3 analysis, charge state-dependent isolation windows were used. For charge state $z = 2$, the MS isolation window was set at 1.2 m/z; for $z = 3$–6, the MS isolation window was set at 0.7 m/z.

Raw files were processed using Integrated Proteomics Pipeline (IP2 v.6.5.5) using the *Homo sapiens* reviewed Uniprot FASTA database (July 2020) with N-Ras substituted for N-Ras[Q61L] for OCI-AML3 samples, or GFP–N-Ras[G12D] for the syngeneic ON samples, with false discovery rate < 1% at the peptide level, and removed identifications from reverse and contaminants database. A minimum of two unique peptides per MS experiment were required. A minimum MS3 reporter ion intensity of 5,000 per control channel (DMSO t_0) for each peptide spectrum match (PSM) was required, and in cases where there were multiple control channels (hydroxylamine experiments and 10-plex time-course experiments), PSMs were discarded if they had a coefficient of variation ≥ 0.5 for the control channels. Relative protein abundance was then averaged across all PSMs.

For hydroxylamine datasets, proteins were required to be quantified in either NB-4 ($n=1$), ON ($n=1$), or at least two experiments for OCI-AML3 studies ($n=2$).

For time-course studies, PSMs were required to have non-zero intensities in all t_0 channels. Additionally, outlier PSMs, having a coefficient of variation ≥ 0.5 for percent of control values on a per channel basis for a particular protein (having three or more PSMs), per experiment, were removed. Proteins were required to be quantified in at least two experiments for OCI-AML3 ($n=3$ individual experiments) and ON studies ($n=4$). For NB-4 studies where 6-plex and 10-plex data were combined, proteins were required to have a standard deviation (across percent control values) of <100 in all studied conditions, and to have been quantified in at least four DMSO t_1 biological replicates (channels).

Stable isotope labeling and SILAC-TMT data processing for protein turnover.
OCI-AML3 cells were grown and passaged six times in SILAC RPMI supplemented with 10% FBS, L-glutamine (2 mM), penicillin (100 U ml⁻¹), streptomycin (100 µg ml⁻¹), 50 µM β-mercaptoethanol, and L-lysine·HCl and L-arginine·HCl (100 µg ml⁻¹ each) or [$^{13}C_6$,$^{15}N_2$]-L-lysine and [$^{13}C_6$,$^{15}N_4$]-L-arginine (100 µg ml⁻¹ each). Cells in 'light' media were pelleted and resuspended at 0.5×10^6 cells ml⁻¹ in 'heavy' media and treated with DMSO or 500 nM ABD957. Cells were counted to determine growth rates and harvested at 3, 6, 24 and 72 h in triplicate (doubling times of 29 and 34 h for DMSO and ABD957-treated cells, respectively). Cells pellets were lysed in DPBS containing protease inhibitors (Roche) and 1 mM PMSF using a Branson Sonifier probe sonicator (three rounds of eight pulses, 40% duty cycle, output setting = 4). Protein concentration was determined by DC assay on a microplate reader, and 200 µg was precipitated with 1 ml of ice-cold acetone followed by centrifugation at 16,000g for 10 min, and protein pellets were washed with 1 ml of ice-cold acetone. Proteomes were resuspended with 50 µl of 8 M urea in 200 mM EPPS (pH 8), reduced with 10 mM dithiothreitol incubated at 65 °C for 15 min. Samples were cooled to room temperature and alkylated with 20 mM iodoacetamide incubated at 37 °C for 30 min. Samples were diluted to 2 M urea by addition of 145 µl of 200 mM EPPS (pH 8) and digested overnight at 37 °C with 4 µg of sequence grade porcine trypsin (Promega) and 1 mM $CaCl_2$. Peptide concentrations from digests were determined by microBCA assay (Thermo Fisher Scientific). TMT labeling and MS were performed as previously described[58]. In brief, for each sample, 25 µg of peptides was transferred to a new Eppendorf tube, and brought up to 35 µl with 200 mM EPPS (pH 8), diluted with 9 µl of acetonitrile, and incubated with 5 µl (20 µg µl⁻¹) of the corresponding 10-plex TMT tag (Thermo Fisher Scientific) at room temperature for 1 h with occasional vortexing. Labeling reaction was quenched with 5 µl of 5% hydroxylamine for 15 min, followed by acidification with 2.5 µl of formic acid. Samples were combined and vacuum-centrifuged to dryness to remove acetonitrile, reconstituted in buffer A (95% H_2O, 5% acetonitrile, 0.1% formic acid) and desalted by passing through Sep-Pak C18 cartridges (55–105 µm, Waters). The eluent was evaporated to dryness, resuspended in buffer A (95% H_2O, 5% acetonitrile, 0.1% formic acid) and fractionated into a 96-deep-well plate using HPLC (Agilent), for offline high pH fractionation. The peptides were eluted on to a capillary column (ZORBAX 300Extend-C18, 3.5 µm) and separated at a flow rate of 0.5 ml min⁻¹. The plate was evaporated to dryness and every 12th fraction concatenated for 12 final fractions (combining every column).

Raw files were processed using Integrated Proteomics Pipeline (IP2 v.6.5.5) using the *Homo sapiens* reviewed Uniprot FASTA database (July 2020) with N-Ras substituted for N-Ras[Q61L]. Samples were simultaneously searched for both light and heavy isotopes specifying the heavy labels as lysine (+8.0142) and arginine (+10.0083). Cysteine carbamidomethylation (+57.02146) and TMT labels to N terminus and lysine (229.1629) were static modifications, and methionine oxidation (+15.994915) was differential allowing one per peptide. Proteins required two unique peptides and false discovery rate < 1% at the peptide level. Data normalization and processing were performed as previously described[30]. In brief, peptides were required to be unique fully tryptic and nonterminal. Light and heavy PSMs were required to have non-zero intensities in the light and heavy channels, respectively. For each individual experiment, intensities for heavy and light peptides were separately row-wise normalized and total sum normalization was then applied. Heavy and light PSMs were required to have a normalized intensity $\geq 2,500$ in heavy and light control channels, respectively. Fractional ratios for each time point versus the corresponding control channel were then calculated. Then, light and heavy fractional ratios at the PSM level were fitted to exponential equations modeling protein synthesis and degradation:

$$\mathrm{ratio_{syn}}(t) = (B_{syn} - A_{syn})\, e^{-K_{syn} t} + A_{syn}$$

$$\mathrm{ratio_{deg}}(t) = (A_{deg} - B_{deg})\, e^{-K_{deg} t} + A_{deg}$$

PSMs were filtered to require the following fitted parameters ranges: K, 0–5; A, 0.67–1.5; B, 0–0.3; they were required to have a coefficient of determination $R^2 \geq 0.7$. PSM ratios across experiments were then grouped per protein and curve fitting and filtering was repeated on the protein level. Half-lives for each protein were calculated after taking into account the different rates of cell doubling (k_{cd}) for each treatment condition using the following equation:

$$T_{1/2} = \frac{\ln 2}{K - k_{cd}}$$

Proliferation assay. A 40 mM stock solution of ABD957 was serially diluted in DMSO to obtain 2,000× concentrations. Next, twice-concentrated medium (2×) was obtained by diluting the drugs 1,000-fold in culture medium. A solvent control was obtained by diluting DMSO 1,000-fold in culture medium. To test the effect of ABD957 on cellular growth, cells were resuspended in fresh culture medium to a concentration of 6×10^5 cells ml⁻¹ and seeded in a 96-well plate (75 µl per plate), or 5,000 cells per well in 50 µl. Subsequently, an equal volume of 2× drugged medium or control was added. Each treatment was performed in triplicate. After 72 h in culture, 50 µl of each well were transferred to a white, flat-bottom 96-well plate and an equal volume of CellTiter Glo reagent was added. After 30 min of shaking at room temperature, luminescence was analyzed using a Tecan Infinite M200PRO or CLARIOstar (BMG Labtech) plate reader. Raw values were normalized using Prism GraphPad software.

Western blot analysis. A minimum of 2×10^6 cells per condition were pelleted and resuspended in fresh medium at 1×10^6 cells ml⁻¹ containing compounds at the indicated concentration. Compound-containing media were obtained by diluting a 1,000-fold concentrated drug stock or vehicle (DMSO control) in fresh medium. Unless otherwise indicated, cells were treated for 4 h, and then pelleted by centrifugation (500g), washed in PBS and frozen. Cells were resuspended in RIPA buffer (Thermo Fisher Scientific) supplemented with PhosSTOP (Sigma-Aldrich) and protease inhibitors (Roche) and lysed using a Branson Sonifier probe sonicator (three rounds of eight pulses, 40% duty cycle, output setting = 4). Lysates were separated on SDS–PAGE tris-glycine gels, and transferred to nitrocellulose membranes at 350 mA for 90 min, blocked and probed with primary and secondary antibodies in 5% milk in 1% TBS-T. Antibodies for western blotting included anti-pan-Ras (Cell Signaling, 3965, 1:500), anti-N-RAS (Santa Cruz, sc-31, 1:1,000), anti-Ras (G12D-specific mutant) (Cell Signaling, 14429, 1:1,000), anti-pERK (Cell Signaling, 4370, 1:1,000), anti-ERK (Cell Signaling, 9107, 1:2,500), anti-HSP90-HRP (Cell Signaling, 79641, 1:5,000), anti-mouse HRP (Cell Signaling, 7076, 1:10,000), anti-rabbit HRP (Cell Signaling 7074 or Santa Cruz sc2030, 1:10,000), LI-COR IRDye 800CW donkey anti-rabbit (1:10,000) and LI-COR IRDye 680RD goat anti-mouse (1:10,000). Blots were imaged on a LI-COR Odyssey (Model 9120) (pERK and ERK) or detected using chemiluminescence on a Bio-Rad ChemiDoc XRS imager. Densitometry analysis was performed using ImageJ software (NIH).

Live-cell imaging and colocalization analysis. ON or ONK control cells (2×10^5) were plated on to 12- or 27-mm Nunc glass bottom dishes the night before imaging and diluted with 400 µl of complete RPMI medium so that the entire glass bottom was covered. For colocalization analysis between GFP–N-Ras[G12D] and RFP–GALNT2, cells were treated with Cell Light Golgi RFP 2.0 reagent (Thermo Fisher Scientific, catalog. no C10593) and incubated overnight and imaged the following day. For colocalization between GFP–N-Ras[G12D] and plasma membrane, the day following plating, cells were diluted to 2 ml with complete RPMI containing Alexa-647-conjugated WGA (Thermo Fisher Scientific, catalog

no. W32466) so that the final concentration was $5\,\mu g\,ml^{-1}$ and transferred to a ZEISS LSM 880 laser scanning confocal microscope equipped with an incubator equilibrated to $37\,°C$ and 5% CO_2 for $10\,min$ before imaging. Cells were imaged using a C-Apochromat ×63/1.2 W autocorr M27 oil objective with an image size of ~$200 × 200\,\mu m^2$. GFP and RFP were excited using a 633 and 488 nm laser, lines and spectral filtering of emission bands was limited to 493–$598\,nm$ for GFP and 639–$755\,nm$ for RFP. For plasma membrane colocalization, images were acquired over five z-planes (~$5\,\mu m$) every 2 min using sequential line scanning for 10 min before compound infusion. After 10 min, medium was infused with ABD957 to the indicated concentration and images collected for an additional 30 min using the same acquisition parameters. For Golgi colocalization, images were acquired at focal planes based on medial Golgi signal and imaged by sequential line scanning. In addition to sampling every 2 min, GFP-only images were acquired by sampling every 1 min over five z-planes (~$1\,\mu m$) using the similar acquisition parameters. Post-acquisition, images were exported as 16-bit TIF files using zen blue and analyzed using the custom cell profiler pipeline 'Correlation_Ras_Lectin_8-19-20.cppipe' or 'Correlation_Ras_Golgi_8-19-20' generated in v.3.1.9. Briefly, cellular objects were identified using minimum cross entropy and offset invariant Pearson correlation between GFP and RFP plasma membrane signal within cellular objects was used for time-course analysis for each optical section collected, using a global threshold value of 15% of maximum[59]. Basal correlation was normalized for direct comparison of change in correlation with time across experiments. Aggregation of biological replicates of time-course experiments was conducted from frames collected at 60 min post compound exposure for each optical section. For Golgi colocalization, cellular objects were selected by minimum cross entropy and Mander's correlation coefficient between the fraction of total intracellular GFP signal that overlapped with the RFP-Golgi signal was calculated for each optical section after global thresholding at 15% of maximum intensity.

CRISPR–Cas9 KO lines. The following single guide RNA (sgRNA) sequences were cloned in the pLX-sgRNA vector (Addgene plasmid no. 50662): 5′-GTCAGAAATACTCACGCATGC-3′, targeting *LYPLA1* (LYPLA1_4); 5′-GACAGCTGCTCACCTGGCACC-3′, targeting *ABHD17A* (ABHD17A_1). OCI-AML3 cells were transduced with either pLX-LYPLA1_4 or pLX-ABHD17A_1, as previously described[56], and selected with blasticidin. The lentiCRISPR v2 vector (Addgene plasmid no. 52961) was modified to replace the puromycin resistance gene with a mCherry marker. Subsequently, the following sgRNA sequences were cloned in lentiCRISPR v2-mCherry: 5′-GGTCCAGTTCAAGACATACCC-3′, targeting *LYPLA2* (LYPLA2_3); 5′-GCATGGCACTGGAGTATGGCC-3′, targeting *LYPLA2* (LYPLA2_4); 5′-GCGAGCAGCAAGATCCACAGA-3′, targeting *ABHD17B* (ABHD17B_4). OCI-AML3 cells transduced with pLX-LYPLA1_4 were transduced with either LYPLA2_3 or LYPLA2_4; OCI-AML3 cells transduced with pLX-ABHD17A_1 were transduced with either ABHD17B_1 or ABHD17B_4. mCherry+ cells were sorted and diluted to 4 cells ml^{-1} to allow isolation of single-cell clones. After expansion, genomic regions around the sgRNA were amplified, cloned into a Zero Blunt TOPO PCR vector (Thermo Fisher Scientific) and sequenced to verify the presence of frameshift-disrupting insertions/deletions. The following knockout clones were identified: LYPLA-DKO 1 (LYPLA1_4+LYPLA2_3), LYPLA-DKO 2 (LYPLA1_4+LYPLA2_4), ABHD17-DKO 1 (ABHD17A_1+ABHD17B_4) and ABHD17-DKO 2 (ABHD17A_1+ABHD17B_4). For all clones, ABPP analysis was used to functionally verify the knockout of respective serine hydrolases (Supplementary Fig. 5a).

Statistical analysis. Unless otherwise stated, quantitative data are expressed in bar and line graphs with mean ± s.d. (error bar) shown. Differences between two groups were examined using an unpaired two-tailed Student's t-test with equal or unequal variance as noted. Significant P values are indicated (*$P < 0.05$, **$P < 0.01$, ***$P < 0.001$ and ****$P < 0.0001$).

Reporting Summary. Further information on the research design is available in the Nature Research Reporting Summary linked to this article.

Data availability
All mass spectrometry data are available via ProteomeXchange with identifier PXD023932. Source data are provided with this paper. All other data that support the findings of this study are available from the corresponding authors upon reasonable request.

Code availability
Code used to process mass spectrometric and imaging data are available on GitHub: https://github.com/cravattlab/remsberg_ncb_2021.

References
49. Patricelli, M. P., Giang, D. K., Stamp, L. M. & Burbaum, J. J. Direct visualization of serine hydrolase activities in complex proteomes using fluorescent active site-directed probes. *Proteomics* **1**, 1067–1071 (2001).
50. Chang, J. W., Cognetta, A. B. 3rd, Niphakis, M. J. & Cravatt, B. F. Proteome-wide reactivity profiling identifies diverse carbamate chemotypes tuned for serine hydrolase inhibition. *ACS Chem. Biol.* **8**, 1590–1599 (2013).
51. Hatfield, M. J. et al. Biochemical and molecular analysis of carboxylesterase-mediated hydrolysis of cocaine and heroin. *Br. J. Pharmacol.* **160**, 1916–1928 (2010).
52. Inloes, J. M. et al. The hereditary spastic paraplegia-related enzyme DDHD2 is a principal brain triglyceride lipase. *Proc. Natl Acad. Sci. USA* **111**, 14924–14929 (2014).
53. Xu, T. et al. ProLuCID: an improved SEQUEST-like algorithm with enhanced sensitivity and specificity. *J. Proteomics* **129**, 16–24 (2015).
54. Cociorva, D., Tabb, D. L. & Yates, J. R. Validation of tandem mass spectrometry database search results using DTASelect. *Curr. Protoc. Bioinformatics* **Chapter 13**, Unit 13.4 (2007).
55. Zuber, J. et al. An integrated approach to dissecting oncogene addiction implicates a Myb-coordinated self-renewal program as essential for leukemia maintenance. *Genes Dev.* **25**, 1628–1640 (2011).
56. Burgess, M. R. et al. Preclinical efficacy of MEK inhibition in Nras-mutant AML. *Blood* **124**, 3947–3955 (2014).
57. Wang, Y. et al. Expedited mapping of the ligandable proteome using fully functionalized enantiomeric probe pairs. *Nat. Chem.* **11**, 1113–1123 (2019).
58. Vinogradova, E. V. et al. An activity-guided map of electrophile–cysteine interactions in primary human T cells. *Cell* **182**, 1009–1026 e29 (2020).
59. Adler, J. & Parmryd, I. Quantifying colocalization by correlation: the pearson correlation coefficient is superior to the Mander's overlap coefficient. *Cytometry A* **77**, 733–742 (2010).

Author contributions
J.R.R., R.M.S., N.A.Z., M.J.N., K.S. and B.F.C. conceived the project and wrote the paper. J.R.R. and M.M.D. performed palmitoyl-proteomics experiments. M.J.N. led efforts to identify ABD957. R.M.S. performed N-Ras palmitoylation assays. N.A.Z., J.R.R., A.J.F., A.I., A.L., M.P. and B.H. performed proliferation and N-Ras signaling assays. T.W.H. performed imaging experiments. A.J.F. developed syngeneic AML cell lines. N.N., C.L.H. and R.M.S. performed gel- and MS-ABPP experiments. N.N. and C.L.H. performed compound characterization and biochemical assays for inhibitor characterization. K.M.L. and R.M.S. analyzed MS-ABPP experiments and analyzed spectra. S.K.R. synthesized Palmostatin M. A.R.H. provided synthetic expertise and contributed to related studies not detailed in this paper. J.R.R., R.M.S., N.A.Z., T.W.H., K.M.L., M.M.D. and M.J.N. performed data analysis and visualization.

Competing interests
The authors declare no competing interests.

Additional information
Extended data are available for this paper at https://doi.org/10.1038/s41589-021-00785-8.

Supplementary information The online version contains supplementary material available at https://doi.org/10.1038/s41589-021-00785-8.

Correspondence and requests for materials should be addressed to M.J.N., K.S. or B.F.C.

Peer review information *Nature Chemical Biology* thanks Matthew Bogyo, Mark Philips and the other, anonymous, reviewer(s) for their contribution to the peer review of this work.

**Reprints and permissions information** is available at www.nature.com/reprints.
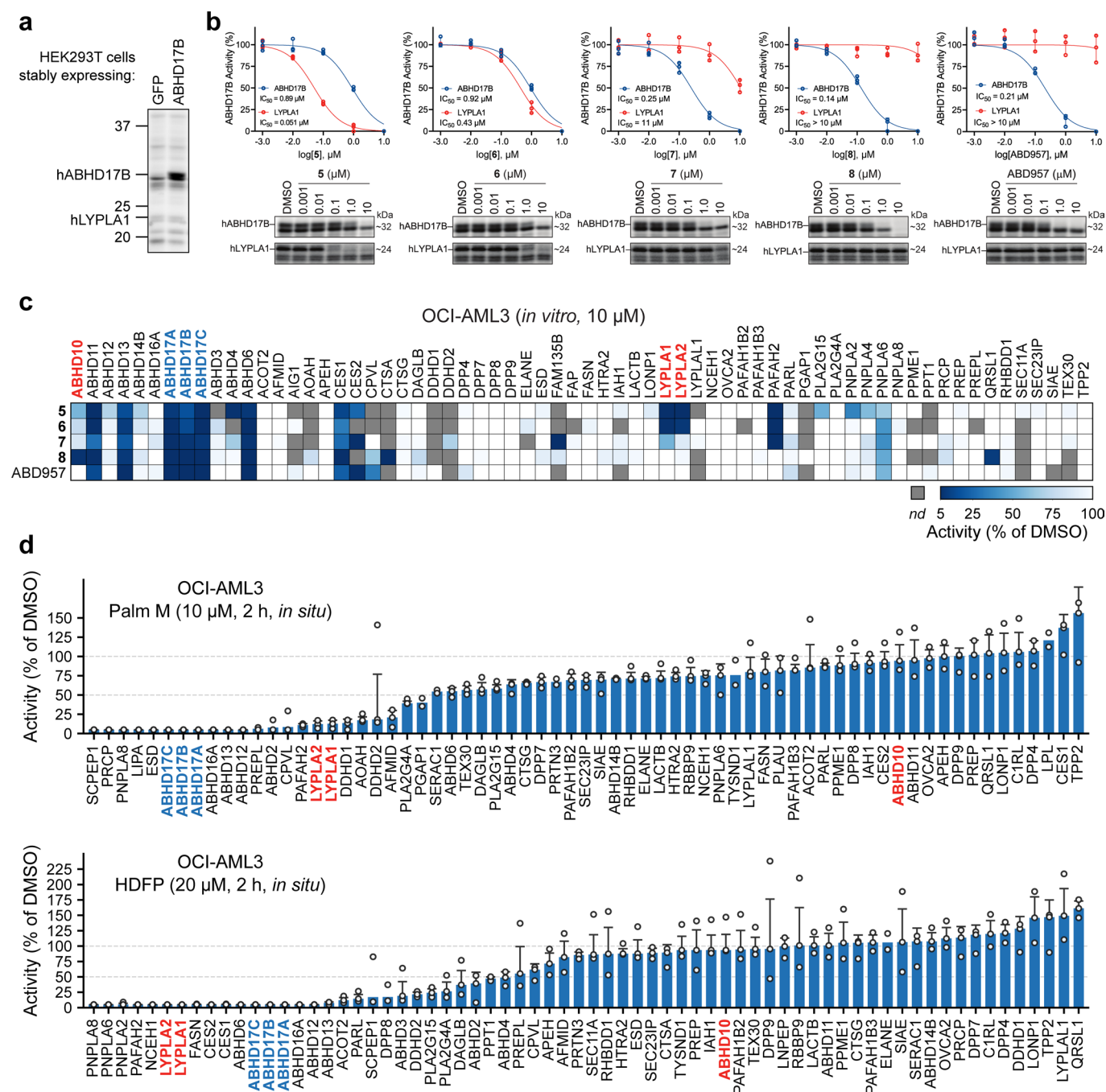
Extended Data Fig. 1 | Characterization of ABHD17 inhibitors. a, Representative gel-ABPP image showing FP-rhodamine labeling of recombinant human ABHD17B (hABHD17B) in proteomic lysates of stably transfected HEK293T cells. **b**, IC_{50} curves and representative gel-ABPP images of human ABHD17B and LYPLA1 activity in HEK293T cell lysate treated with compounds **5–8** and ABD957 for 30 min. Data represent average values ± s.d. (n = 3 independent experiments). **c**, MS-ABPP data of serine hydrolase activities in the particulate fraction of OCI-AML3 proteomes treated with compounds **5-8** and ABD957 for 30 min (10 μM). Data are from single experiments performed at the indicated concentrations for each compound. **d**, MS-ABPP data of serine hydrolase activities in OCI-AML3 cells treated in situ with Palm M (10 μM) or HDFP (20 μM) for 2 h. Data represent the median from three experiments corresponding to independent treatments of cells with compound (Palm M or HDFP) and error bars represent s.d.

a

9 (JJH254)
LYPLA1/2 inhibitor

10 (ABD298)
ABHD13 inhibitor

b

c

d

e
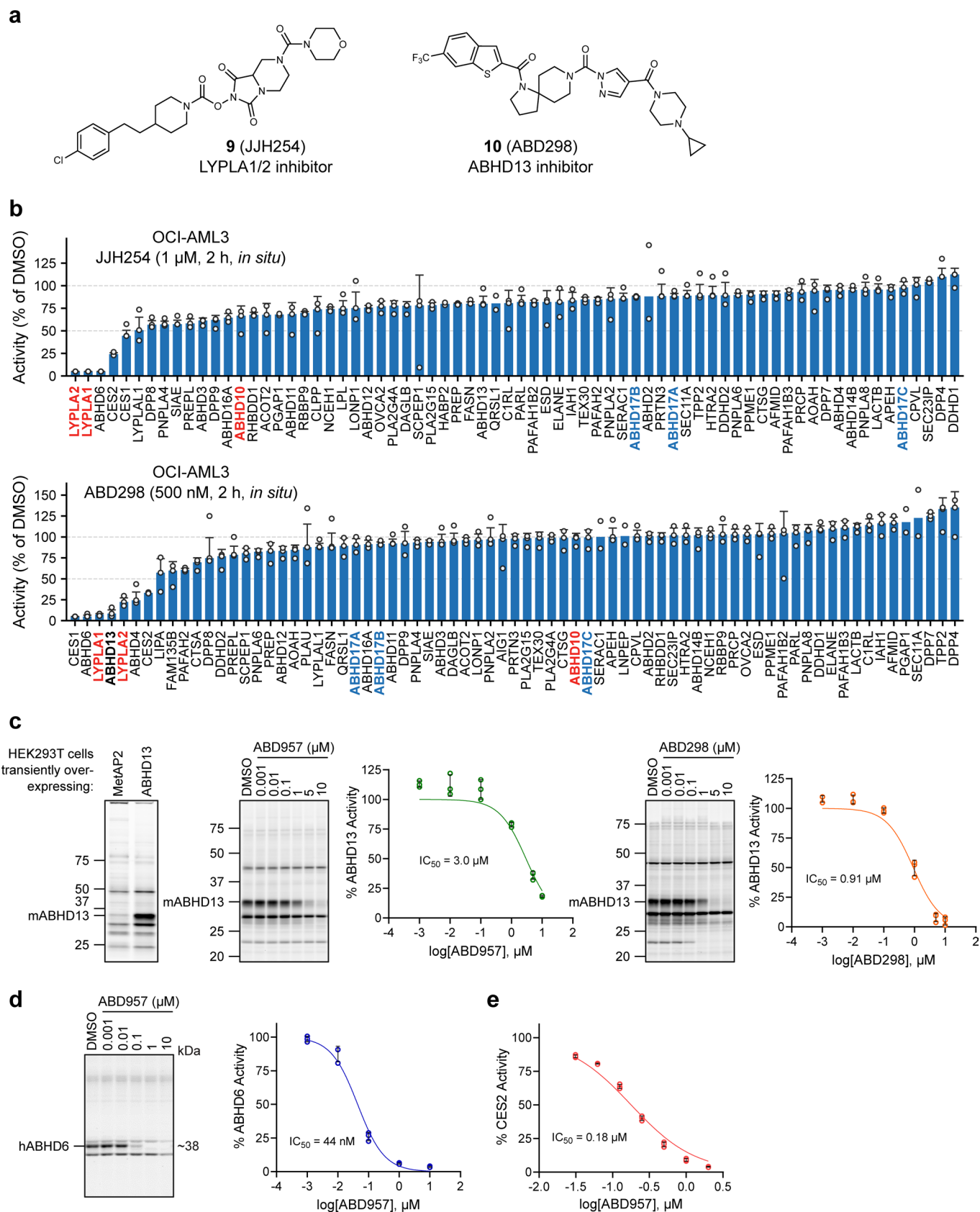
Extended Data Fig. 2 | See next page for caption.

Extended Data Fig. 2 | Analysis of off-targets of ABD957 and control probes accounting for these serine hydrolases. a, Structures of ABD298, an ABHD13 inhibitor, and JJH254, a previously reported LYPLA1/2 inhibitor[25]. **b**, MS-ABPP data of serine hydrolase activities in OCI-AML3 cells treated in situ with JJH254 (1 μM) or ABD298 (500 nM) for 2 h. Data represent the median from three experiments corresponding to independent treatments of cells with each compound (JJH254 or ABD298) and error bars represent standard deviation. **c**, IC_{50} curves and representative gel-ABPP images for ABD957 and ABD298 determined in proteomes of HEK293T cells expressing recombinant mouse ABHD13. Lysates were treated in vitro with inhibitor for 30 min at 37 °C, followed by incubation with FP-Rh for 30 min, RT. Experiments were performed in triplicate. Error bars represent s.d. and center around the mean. **d**, IC_{50} curve and representative gel-ABPP image for ABD957 determined for endogenous human ABHD6 in PC3 cell proteomes following a 30 min inhibitor treatment. Experiments were performed in triplicate. Error bars represent s.d. and center around the mean. **e**, IC_{50} curve for ABD957 derived by measuring the CES2-dependent rate of hydrolysis (background substracted) of the substrate 4-nitrophenyl acetate (pNPA) in proteomes of HEK293T cells expressing recombinant human CES2 following a 30 min inhibitor treatment. The mean reaction velocity (V_{mean}, ΔAbs / min·μg protein) in mock- versus CES2-transfected proteomes was 8.7 ± 1.9 min^{-1}·μg^{-1} and 31 ± 1.2 $^{min^{-1}, μg^{-1}}$, respectively. Data presented for all IC_{50} determinations represent average values $\pm$ s.d. (n = 3 independent experiments).
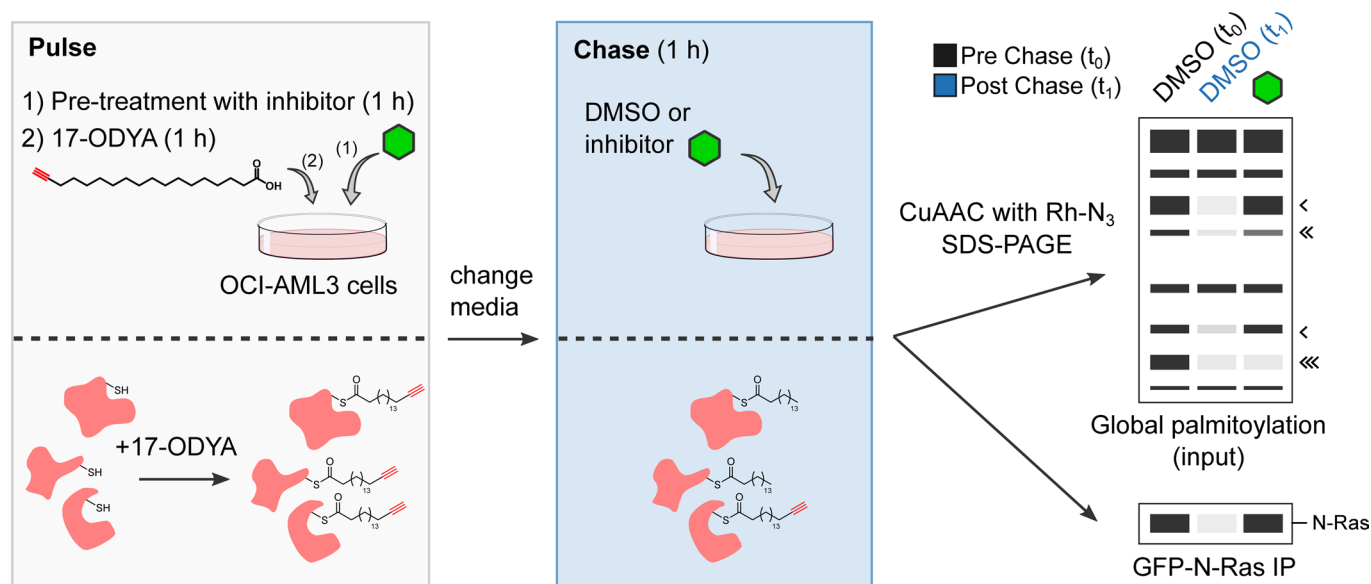
Extended Data Fig. 3 | Schematic of a dynamic palmitoylation assay using metabolic labeling with 17-ODYA. Black arrowheads next to mock gel mark proteins that show dynamic palmitoylation fully (one arrowhead), partially (two arrowheads), or not (three arrowheads) preserved by serine hydrolase inhibition.

a

b

c

d
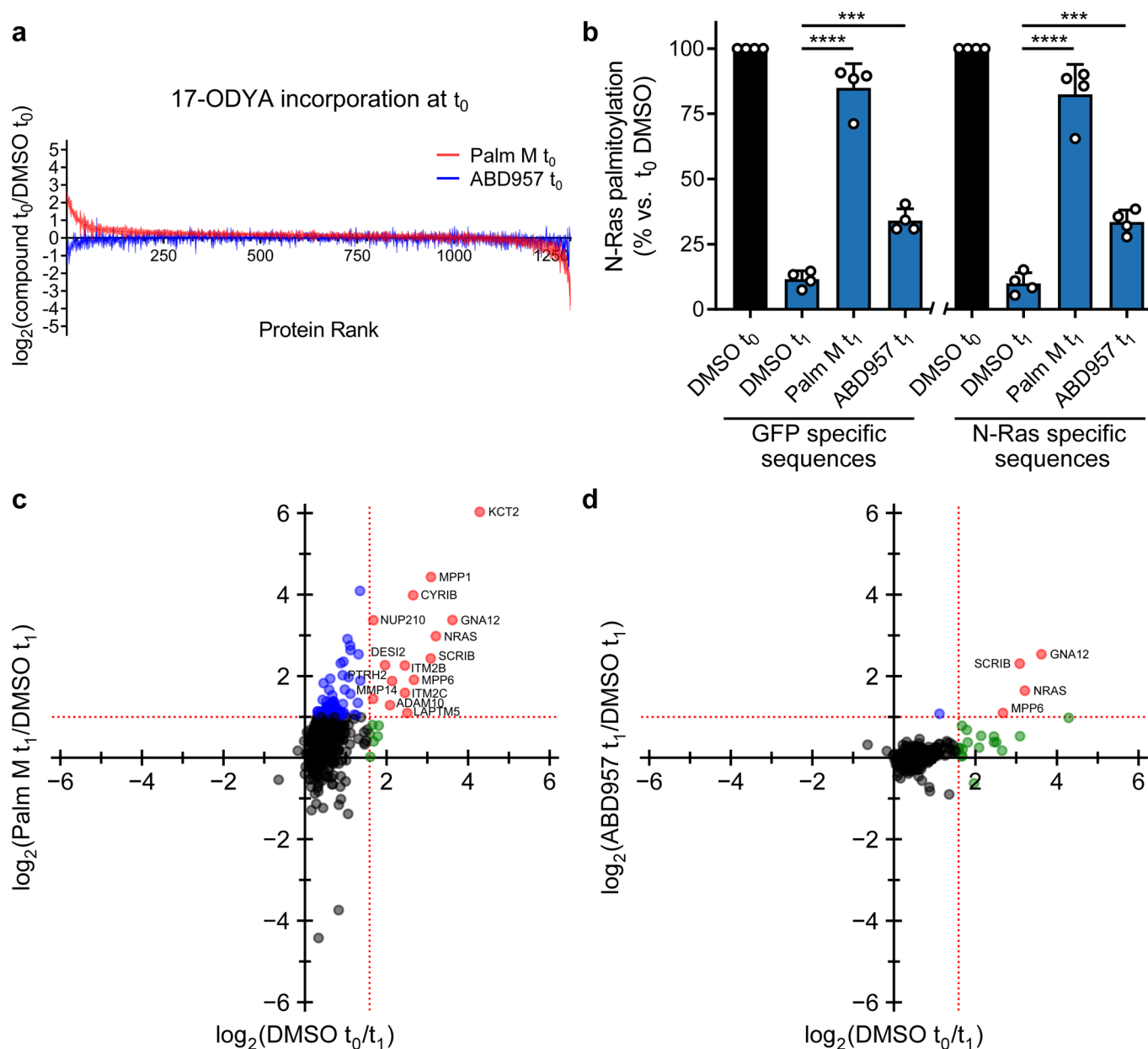
Extended Data Fig. 4 | Global palmitoylation effects of Palm M and ABD957 in leukemia cells. a, MS-based proteomics in OCI-AML3 cells showing the 17- ODYA labeling at t_0. The results indicate that Palm M increases the apparent palmitoylation state of several proteins prior to the chase period and, as shown in Fig. 3a, some of these proteins are not dynamically palmitoylated (blue proteins in Fig. 3a). **b**, Bar graph quantifying different categories of N-Ras peptides from MS-based proteomics experiments in ON cells. Data represent average values relative to DMSO $t_0 \pm$ s.d. (n = 4 from two biological replicates). Statistical significance was calculated with unpaired two-tailed Student's t-test with equal variance, ***$P < 0.001$, ****$P < 0.0001$ represent significant increase compared to DMSO t1 (also see Supplementary Dataset 3). P values were 5.5×10^{-5} (Palm M GFP specific), 1.8×10^{-4} (ABD957 GFP specific), 2.1×10^{-5} (Palm M N-Ras specific), 2.7×10^{-4} (ABD957 N-Ras specific). **c, d**, Scatter plots as described in Fig. 3a in ON cells.
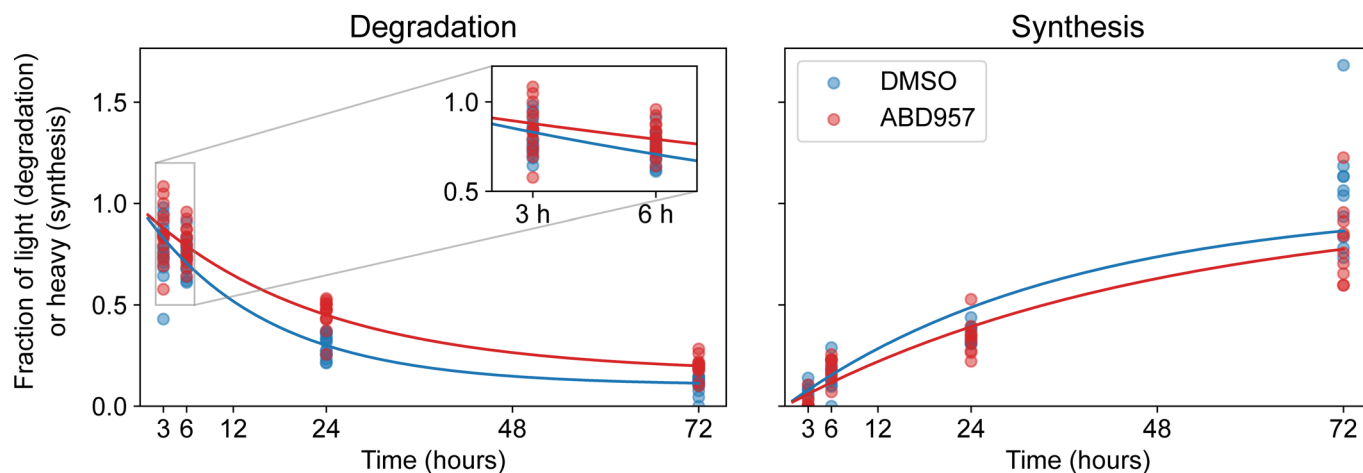
Extended Data Fig. 5 | Effects of ABD957 treatment on N-Ras turnover in OCI-AML3 cells. a, Degradation and synthesis curves for N-Ras in OCI-AML3 cells treated with DMSO or ABD957 (500 nM). Each dot represents a peptide spectrum match (PSM) from one of three biological replicates. OCI-AML3 cells grown in light SILAC media were pelleted and resuspended in heavy SILAC media containing DMSO or ABD957 and harvested at the indicated times. Also see Supplementary Dataset 4.
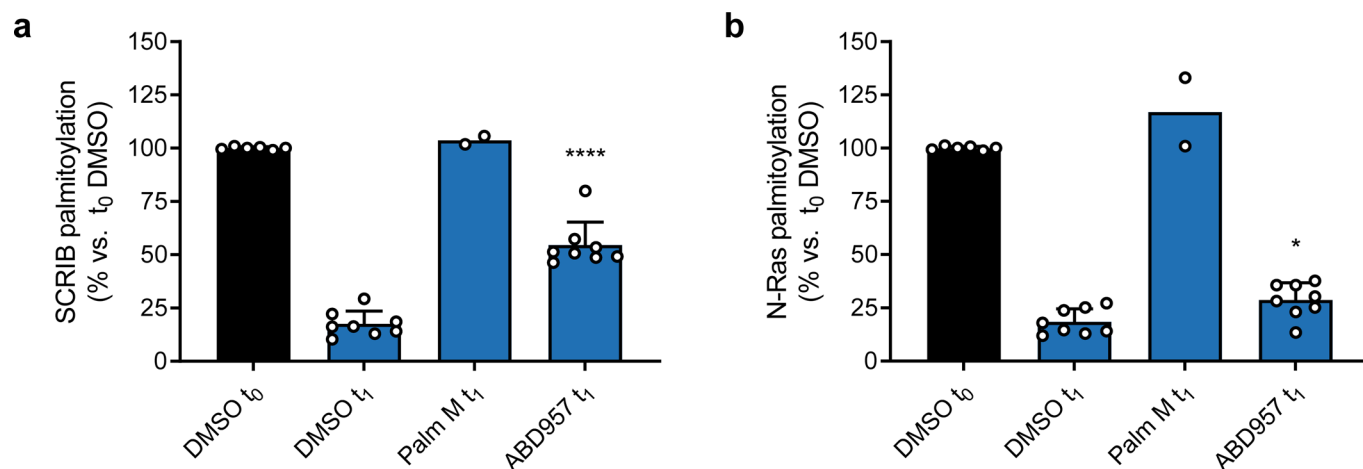
Extended Data Fig. 6 | Global palmitoylation effects of Palm M and ABD957 in NB-4 cells. a, b, Bar graphs quantifying SCRIB and N-Ras palmitoylation from MS-based proteomic experiments in NB-4 cells. Data represent average values relative to DMSO t_0 ± s.d. (biological replicates; n=2 for Palm M t_1, n=8 for all other conditions). Statistical significance was calculated with unpaired two-tailed Student's t-test with equal variance, *$P < 0.05$, ****$P < 0.0001$ represent significant increase compared to DMSO t_1 (also see Supplementary Dataset 2 and 3). P values were 6.5×10^{-7} (SCRIB), 0.013 (N-Ras).
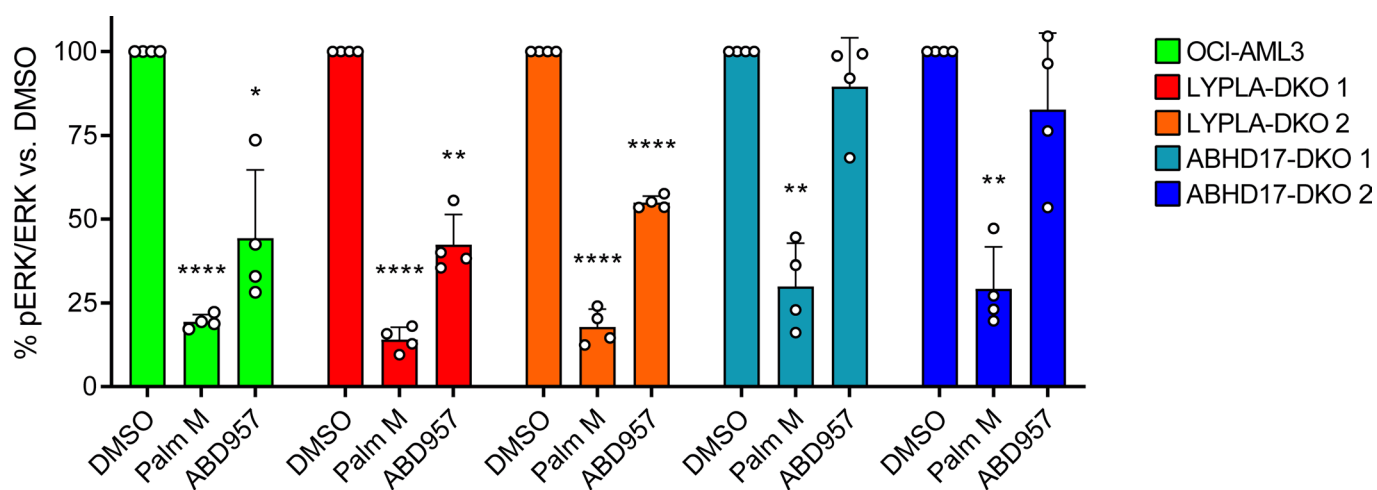
Extended Data Fig. 7 | Quantification of data shown in Fig. 5f; average values ± s.d. (n = 4 independent experiments). Statistical significance was calculated with unpaired two-tailed Student's *t*-test with unequal variance compared to DMSO control, *$P < 0.05$, **$P < 0.01$, ****$P < 0.0001$. *P* values were 4.8×10^{-6} (Palm M OCI-AML3), 0.012 (ABD957 OCI-AML3), 0.0016 (Palm M ABHD17-DKO 1), 0.0014 (Palm M ABHD17-DKO 2), 2.2×10^{-5} (Palm M LYPLA-DKO 1), 0.0010 (ABD957 LYPLA-DKO 1), 7.4×10^{-5} (Palm M LYPLA-DKO 2), 2.1×10^{-5} (ABD957 LYPLA-DKO 2).

a

b
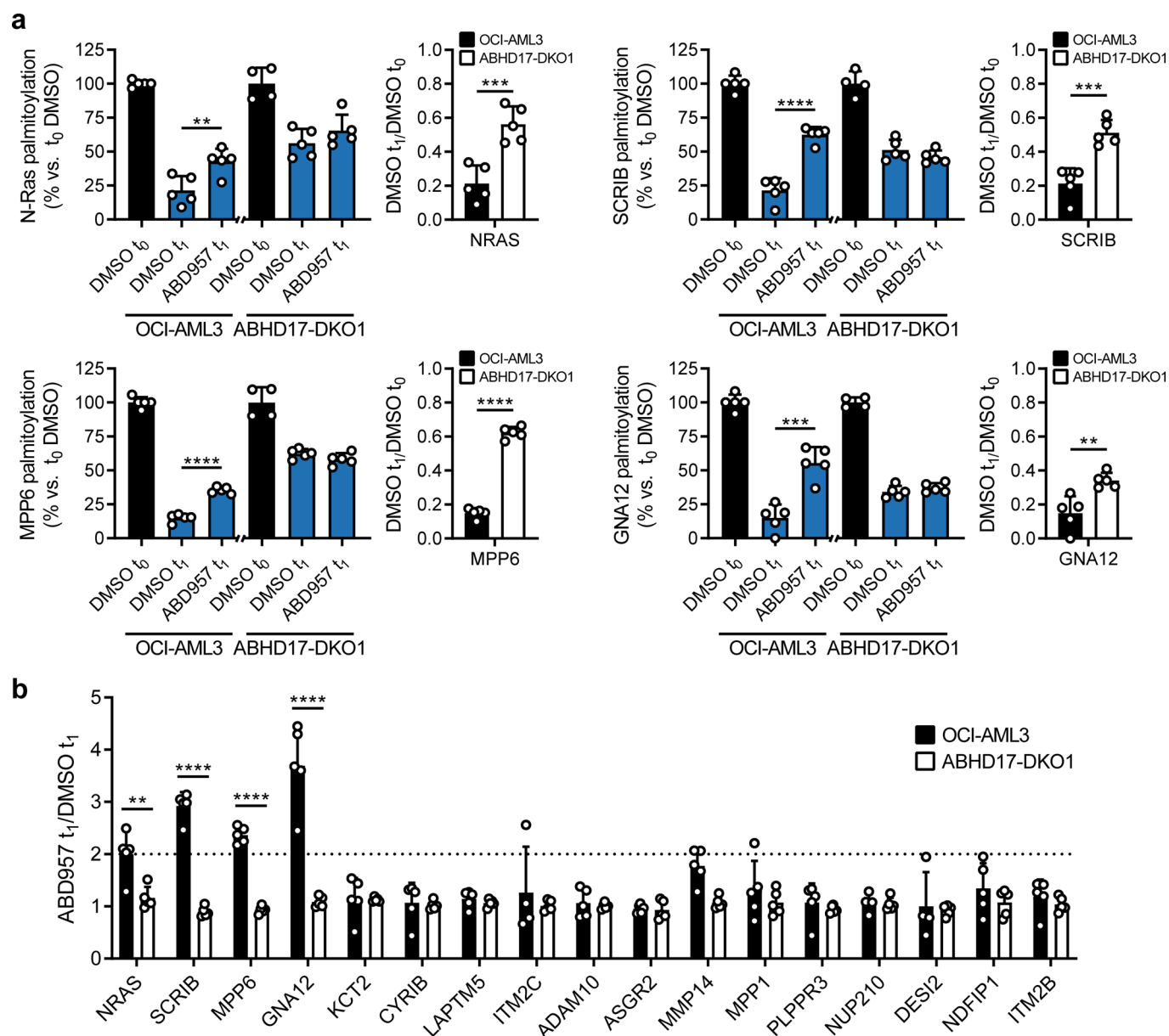
Extended Data Fig. 8 | MS-based proteomic analysis of dynamic palmitoylation in parental and ABHD17- DKO cells. a, Profiles for ABD957-regulated palmitoylated proteins from mass spectrometry (MS)-based experiments of OCI-AML3 and ABHD17-DKO 1 cells performed as described in Extended Data Fig. 3. Cells were preincubated with ABD957 (500 nM) or DMSO for 1h, metabolically labeled with 20 μM 17-ODYA for 1h (t_0) and chased with media lacking 17-ODYA for 1 h (t_1) containing ABD957 (500 nM) or DMSO control. Data represent average values relative to each cell lines corresponding DMSO t_0 control ± s.d. (biological replicates, n = 4 for DMSO t_0 values, n=5 for all others). Statistical significance was calculated with unpaired two-tailed Student's t-test with equal variance, *$P < 0.05$, **$P < 0.01$, ***$P < 0.001$, ****$P < 0.0001$, compared to DMSO t_1 for left panels or compared to DMSO t_1/t_0 ratio between OCI-AML3 and ABHD17-DKO 1 cells for right panels. P values were 0.0096 (OCI-AML3 ABD957 N-Ras), 7.8×10^{-4} (OCI- AML3 DMSO t_1/t_0 N-Ras), 2.4×10^{-5} (OCI-AML3 ABD957 SCRIB), 4.4×10^{-4} (OCI-AML3 DMSO t_1/t_0 SCRIB), 1.9×10^{-6} (OCI-AML3 ABD957 MPP6), 1.2×10^{-8} (OCI-AML3 DMSO t_1/t_0 MPP6), 3.9×10^{-4} (OCI-AML3 ABD957 GNA12), 0.0044 (OCI-AML3 DMSO t_1/t_0 GNA12). **b**, Effect of ABD957 on dynamically palmitoylated proteins in OCI-AML3 and ABHD17-DKO 1 cells. Data represent average values ± s.d. (n = 5 biological replicates). Statistical significance was calculated for proteins with >2-fold increases in ABD957-treated OCI-AML3 cells with unpaired two-tailed Student's t-test with equal variance, **$P < 0.01$, ****$P < 0.0001$ compared to ABHD17-DKO 1 cells. P values were 0.0049 (N-Ras), 2.3×10^{-7} (SCRIB), 7.6×10^{-8} (MPP6), 8.1×10^{-5} (GNA12).

nature research

Corresponding author(s): Micah J. Niphakis, Kevin Shannon, Benjamin F. Cravatt

Last updated by author(s): 03/01/2021

Reporting Summary

Nature Research wishes to improve the reproducibility of the work that we publish. This form provides structure for consistency and transparency in reporting. For further information on Nature Research policies, see Authors & Referees and the Editorial Policy Checklist.

Statistics

For all statistical analyses, confirm that the following items are present in the figure legend, table legend, main text, or Methods section.

n/a	Confirmed	
☐	☒	The exact sample size (*n*) for each experimental group/condition, given as a discrete number and unit of measurement
☐	☒	A statement on whether measurements were taken from distinct samples or whether the same sample was measured repeatedly
☐	☒	The statistical test(s) used AND whether they are one- or two-sided *Only common tests should be described solely by name; describe more complex techniques in the Methods section.*
☒	☐	A description of all covariates tested
☒	☐	A description of any assumptions or corrections, such as tests of normality and adjustment for multiple comparisons
☐	☒	A full description of the statistical parameters including central tendency (e.g. means) or other basic estimates (e.g. regression coefficient) AND variation (e.g. standard deviation) or associated estimates of uncertainty (e.g. confidence intervals)
☐	☒	For null hypothesis testing, the test statistic (e.g. *F*, *t*, *r*) with confidence intervals, effect sizes, degrees of freedom and *P* value noted *Give P values as exact values whenever suitable.*
☒	☐	For Bayesian analysis, information on the choice of priors and Markov chain Monte Carlo settings
☒	☐	For hierarchical and complex designs, identification of the appropriate level for tests and full reporting of outcomes
☒	☐	Estimates of effect sizes (e.g. Cohen's *d*, Pearson's *r*), indicating how they were calculated

Our web collection on statistics for biologists contains articles on many of the points above.

Software and code

Policy information about availability of computer code

Data collection	ZEISS LSM 880 laser scanning confocal microscope was used for fluorescence live-cell data collection. Xcalibur v2.2 was used for mass spectrometry data collection. Tecan Infinite M200PRO or CLARIOstar (BMG Labtech) was used for cell viability data collection. Li-cor Odyssey (Model 9120) and Bio-Rad ChemiDocTM XRS imager were used for blotting data collection.
Data analysis	IP2 v6.5.5, RawConverter v1.1.0.22, ProLuCID v1.4, and CIMAGE were used to analyze MS-ABPP data. Skyline v20.1 was used to analyze PRM data. IP2 v6.5.5 and ProLuCID v1.4 were used to analyze quantitative TMT data. ImageJ 2.0 was used to analyze western blot and gel-based palmitoylation data. CellProfiler v3.1.9 was used to analyze and quantify fluorescence live-cell imaging data. GraphPad Prism v8.01 was used to perform statistical tests and generate all the bar and line graphs.

For manuscripts utilizing custom algorithms or software that are central to the research but not yet described in published literature, software must be made available to editors/reviewers. We strongly encourage code deposition in a community repository (e.g. GitHub). See the Nature Research guidelines for submitting code & software for further information.

Data

Policy information about availability of data

All manuscripts must include a data availability statement. This statement should provide the following information, where applicable:

- Accession codes, unique identifiers, or web links for publicly available datasets
- A list of figures that have associated raw data
- A description of any restrictions on data availability

All mass spectrometry data and Uniprot fasta databases are available via ProteomeXchange with identifier PXD023932. Code used to process mass spectrometric and imaging data are available on GitHub (https://github.com/cravattlab/remsberg_ncb_2021). All other data that support the findings of this study are available from the corresponding authors upon reasonable request.

Field-specific reporting

Please select the one below that is the best fit for your research. If you are not sure, read the appropriate sections before making your selection.

☒ Life sciences   ☐ Behavioural & social sciences   ☐ Ecological, evolutionary & environmental sciences

For a reference copy of the document with all sections, see nature.com/documents/nr-reporting-summary-flat.pdf

Life sciences study design

All studies must disclose on these points even when the disclosure is negative.

Sample size	No statistical methods were used to pre-determine sample size. Where possible, for gel- and MS-based dynamic palmitoylation experiments we aimed for 3 independent replicates, adding more if additional conditions were added during the review process.
Data exclusions	No data was excluded.
Replication	The exact number of experiment replications are noted in the figure legends.
Randomization	Mammalian cells used for this study were grown under identical conditions, so randomization was not used.
Blinding	Mammalian cells used for this study were grown under identical conditions, so blinding was not used.

Reporting for specific materials, systems and methods

We require information from authors about some types of materials, experimental systems and methods used in many studies. Here, indicate whether each material, system or method listed is relevant to your study. If you are not sure if a list item applies to your research, read the appropriate section before selecting a response.

Materials & experimental systems

n/a	Involved in the study
☐	☒ Antibodies
☐	☒ Eukaryotic cell lines
☒	☐ Palaeontology
☒	☐ Animals and other organisms
☒	☐ Human research participants
☒	☐ Clinical data

Methods

n/a	Involved in the study
☒	☐ ChIP-seq
☒	☐ Flow cytometry
☒	☐ MRI-based neuroimaging

Antibodies

Antibodies used	Anti-pan-Ras, Cell Signaling, cat# 3965, 1:500 dilution; Anti-N-RAS (F155), Santa Cruz, cat# sc-31, 1:1000 dilution; Anti-Ras (G12D specific mutant) (D8H7), Cell Signaling, cat# 14429, 1:1000 dilution; Anti-pERK (D13.14.4E), Cell Signaling, cat# 4370, 1:1000 dilution; Anti-ERK (3A7), Cell Signaling, cat# 9107, 1:2500 dilution; Anti-HSP90 (C45G5) HRP conjugate, Cell Signaling, cat#79641, 1:5000 dilution; Anti-mouse IgG, HRP-linked, Cell Signaling, cat# 7076, 1:10,000 dilution; Anti-rabbit IgG, HRP-linked, Cell Signaling, cat# 7074 or Santa Cruz sc-2030, 1:10,000 dilution; Li-cor IRDye 800CW Donkey anti-rabbit, 1:10,000 dilution; Li-cor IRDye 680RD Goat anti-mouse, 1:10,000 dilution; Anti-GFP antibody (Sepharose), cat# ab69314, 1:40 v/v dilution.
Validation	Anti-pan-Ras, Cell Signaling, cat# 3965, 1:500 dilution: validated for western blotting by manufacturer using extracts from HT-29, PAE, NIH-3T3, AR42J, PC12 and C6 cell lysates; Anti-N-RAS (F155), Santa Cruz, cat# sc-31, 1:1000 dilution: validated for western blotting by manufacturer using HeLa, A-431, Jurkat, and NIH/3T3 whole cell lysates; Anti-Ras (G12D specific mutant) (D8H7), Cell Signaling, cat# 14429, 1:1000 dilution: validated for western blotting by manufacturer using THP1, LS174T, HCT116, SW620, NCI-H358, NCI-H1703, and NCI-H1650 whole cell lysates; Anti-pERK (D13.14.4E), Cell Signaling, cat# 4370, 1:1000 dilution: validated for western blotting by manufacturer using whole cell lysates from COS cells, untreated or treated with either U0126 #9903 (10 μM for 1 h) or TPA #4174 (200 nM for 10 min); Anti-ERK (3A7), Cell Signaling, cat# 9107, 1:2500 dilution: validated for western blotting by manufacturer using whole cell lysates from COS cells, untreated or treated with either U0126 #9903 (10 μM for 1 h) or TPA #4174 (200 nM for 10 min); Anti-HSP90 (C45G5) HRP conjugate, Cell Signaling, cat#79641, 1:5000 dilution: validated for western blotting by manufacturer using HeLa, NIH/3T3, and COS-7 whole cell lysates.

Eukaryotic cell lines

Cell line source(s)	OCI-AML3 (DSMZ: ACC-582), NB-4 (DSMZ: ACC-207), NOMO1 (DSMZ: ACC-542), HEK293T (ATCC: CRL-3216), THP1 (ATCC: TIB-202), PC3 (ATCC: CRL-1435), HL60 (DSMZ: ACC-3)
Authentication	All cell lines were authenticated by short tandem repeat loci (STRs) profiling by vendors.
Mycoplasma contamination	All cell lines used in this study were tested negative for mycoplasma.
Commonly misidentified lines (See ICLAC register)	No commonly misidentified cell lines were used in this study.